A second-order accurate, unconditionally energy stable numerical scheme for binary fluid flows on arbitrarily curved surfaces

Qing Xia, Qian Yu, Yibao Li[*]

School of Mathematics and Statistics, Xi'an Jiaotong University, Xi'an 710049, China

Abstract

In this paper, a second-order temporal and spatial accurate, unconditionally energy stable scheme for the binary fluid flows model on arbitrarily curved surfaces is proposed. We construct a novel surface discrete finite volume method for the surface computation with second-order spatial accuracy. The discretization can be obtained based on the surface mesh consisting of triangular grids. In order to obtain second order temporal accuracy, we apply a Crank–Nicolson-type method to the Cahn–Hilliard–Navier–Stokes system under the projection framework. The resulting system is solved by the Jacobi-type iteration method and bi-conjugate gradient stabilized method. The proposed scheme is proved to be unconditionally energy stable, which implies that a larger time step can be used. Additionally, our scheme has been proved to satisfy mass conservation property. Various numerical experiments are presented to demonstrate the efficiency and robustness of the proposed method.
© 2021 Elsevier B.V. All rights reserved.

1. Introduction

Cahn–Hilliard(CH) equation coupled with incompressible Navier–Stokes (NS) equation has received increasing attention across a number of disciplines [1–8]. The complicated system, Cahn–Hilliard–Navier–Stokes (CHNS) system, is proposed as an alternative of sharp interface model since a topological change of the interface can be implicitly captured [9–11]. Various approaches have been proposed to improve the efficiency and stability of the numerical scheme. Kim et al. [12] used a conservative, second-order accurate fully implicit CHNS system. They established a multigrid iterative solver for the nonlinear term and decoupled the pressure term based on the projection method [13]. Han et al. [14] came up with the scheme of solving the CH equation based on a convex splitting method and solving the NS equation by a pressure-projection method. Shen and Yang [15,16] derived a phase-field model for binary fluid flows with large density and viscosity ratio. Guo et al. [17] developed a C^0 finite element formulation for the quasi-incompressible CHNS system and significantly reduced the computation costs while resolving the characteristics of the flow. They avoided using C^{-1} finite element, but simply used C^0 finite

---

* Corresponding author.
  E-mail address: yibaoli@xjtu.edu.cn (Y. Li).
  URL: http://gr.xjtu.edu.cn/web/yibaoli (Y. Li).

element to derive a discrete energy law for the quasi-incompressible CHNS system. Furthermore, various numerical approaches for solving the hybrid system have been developed [18–24]. Although these numerical methods work well for the CHNS system in rectangular or cuboid domains, the evolution of dynamic flows on arbitrarily curved surface is still a tough challenge.

The numerical approximation of partial differential equations on arbitrary surfaces has received extensive attention. To solve the diffusion equations over triangular surface meshes, Chen and Wu [25–27] used a discrete approximation to replace the Laplace–Beltrami operators on the regular surfaces and discussed the discrete divergence theorem and conservation laws from the viewpoint of duality. Under their framework, the partial derivatives of functions can be directly computed in an intrinsic and unified way. Ruuth and Merriman [28,29] proposed the closest point method, which discretized the partial differential equations by a fixed Cartesian grid in the embedding space. This method can treat arbitrary surfaces not limited to closed surface by involving only the standard Cartesian differential operators. Macdonald et al. [30] proposed an novel algorithm for determining eigenvalues and eigenfunctions of the Laplace–Beltrami operator on the general curved surface based on the closest point method.

The main challenge is how to obtain high accuracy computing results for multi-coupled systems on the arbitrarily curved surfaces [31]. Desbrun et al. [32] discretized the NS equations through the discrete exterior calculus framework, which has the differences mainly in the convective term discretization. This method was employed with an interpolation scheme based on Kelvin's circulation theorem and was capable of simulating flows over curved surfaces. Mohamed et al. [33] developed the discrete exterior calculus framework, which used an algebraic discretization of the interior product operator and discretized the combination of wedge product. Reuther and Voigt [34] proposed a surface finite element method for the incompressible NS equation on surfaces, which required the standard ingredients of classical finite element implementations. Yang et al. [35,36] applied a staggered marker-and-cell mesh, which stored the pressure and phase variable at the center of cells. This method was easy to implement with the loss of accuracy and the disappearance of the energy dissipation law. The general surface calculation methods involve non curved points in higher dimensional space.

In this paper, we aim to develop a simple and efficient numerical scheme for CHNS hybrid system on complex surfaces. A fully discrete, unconditionally energy stable numerical scheme for binary fluid flows on arbitrarily curved surfaces, which has second-order temporal and spatial accuracy, will be proposed. A novel surface discrete finite volume method will be constructed for the high accuracy surface computation. It has to be pointed that we focus on the study on the fixed curved surfaces. Based on the NS flow on surfaces or manifolds of the existing studies [14,33–41], we summarize the CHNS model for the arbitrarily curved surfaces. The discrete operators, i.e., discrete gradient, divergence and Laplace–Beltrami operators, are established for the numerical computation. These operators are obtained by the second-order Taylor expansion in discrete space. We apply a Crank–Nicolson-type discretization for the coupled CHNS system under the projection framework to obtain second-order temporal accuracy. Here we use a biconjugate gradient stabilized method for the resulting system of discrete equations. To our best knowledge, this is the first study focusing on binary incompressible fluid flows by the direct discrete method which is second temporal and spatial accuracy and satisfies the unconditional energy stability. Various numerical experiments will be presented to validate the performance of our proposed scheme.

The remainder of this paper is organized as follows: in Section 2, we review the CHNS system, which is resulted from the energetic variation of the action functional of the total hybrid energy. In Section 3, we estimate the discrete gradient operator with second-order spatial accuracy and optimize the discrete divergence and Laplacian–Beltrami operators. Then we describe the discrete CHNS scheme with second-order temporal accuracy based on a Crank–Nicolson-type method. In Section 4, we present the numerical solutions for the incompressible NS equation and the conservative CH equation. Section 5 is devoted to present various numerical experiments. Finally, a concluding remark is drawn in Section 6.

2. Cahn–Hilliard–Navier–Stokes system on arbitrarily curved surfaces

Let us consider the dimensionless incompressible CHNS system on a fixed curved surface $S \subset \mathbb{R}^3$ as in [37–39]:

$$\partial_t \phi(\mathbf{x}, t) + \nabla_S \cdot (\phi(\mathbf{x}, t)\mathbf{v}(\mathbf{x}, t)) = \frac{1}{Pe} \Delta_S \mu(\mathbf{x}, t),$$

$$\mu(\mathbf{x}, t) = f'(\phi(\mathbf{x}, t)) - \epsilon^2 \Delta_S \phi(\mathbf{x}, t),$$

$$\rho \left(\frac{\partial \mathbf{v}(\mathbf{x}, t)}{\partial t} \right) + \rho \left(\frac{\mathbf{v}(\mathbf{x}, t) \cdot \nabla_S \mathbf{v}(\mathbf{x}, t)}{2} \right) + \rho \left(\frac{\nabla_S \cdot (\mathbf{v}(\mathbf{x}, t) \otimes \mathbf{v}(\mathbf{x}, t))}{2} \right) \tag{1}$$

$$= -\nabla_S p(\mathbf{x}, t) + \nabla_S \cdot (\eta \nabla_S \mathbf{v}(\mathbf{x}, t)) - \frac{\sigma}{\epsilon} \phi(\mathbf{x}, t) \nabla_S \mu(\mathbf{x}, t),$$

$$\nabla_S \cdot \mathbf{v}(\mathbf{x}, t) = 0.$$

Here ∇_S, $\nabla_S\cdot$ and Δ_S denote the tangential gradient operator, tangential divergence operator and tangential Laplacian–Beltrami operator, respectively. We use $\mathbf{v} = (u(\mathbf{x}, t), v(\mathbf{x}, t), w(\mathbf{x}, t))$ to denote the velocity field of fluid mixtures, $\phi(\mathbf{x}, t)$ denotes the phase variable. $p(\mathbf{x}, t)$, $\mu(\mathbf{x}, t)$, ρ and η are pressure, chemical potential, density and viscosity, respectively. The term $\mathbf{v}(\mathbf{x}, t) \otimes \mathbf{v}(\mathbf{x}, t)$ is the tensor product. In addition, the dimensionless parameters ϵ, σ and Pe are positive constants. In this paper, we only consider the fixed surfaces with closed property, so there is no boundary conditions for this system. The total energy of the hydrodynamic system includes two parts: the kinetic energy(E_k) and the Ginzburg–Landau type of Helmholtz free energy(E_h)[42,43], which can be written as:

$$E = E_k + E_h = \int_S \left(\frac{\rho |\mathbf{v}(\mathbf{x}, t)|^2}{2} + \rho \left(\frac{\sigma \epsilon}{2} |\nabla_S \phi(\mathbf{x}, t)|^2 + \frac{\sigma}{\epsilon} f(\phi(\mathbf{x}, t)) \right) \right) d\mathbf{x}, \tag{2}$$

where $f(\phi) = \phi^2(1 - \phi)^2/4$ is the double well bulk energy and represents the hydro-phobic type of interactions. The hybrid energy is derived through an energetic variational procedure based on entropy production [17]. With the solution of Eq. (1), the energy dissipation law can be obtained as follows:

$$\frac{dE}{dt} = \rho (\mathbf{v}, \mathbf{v}_t) + \frac{\rho \sigma}{\epsilon} (\mu, \phi_t) = \rho \left(\mathbf{v}, -\nabla_S p + \eta \Delta_S \mathbf{v} - \frac{\sigma}{\epsilon} \phi \nabla_S \mu \right) - \frac{\sigma \rho}{\epsilon Pe} (\nabla_S \mu, \nabla_S \mu) - \frac{\sigma \rho}{\epsilon} (\mu, \nabla_S \cdot (\phi \mathbf{v}))$$

$$= \rho (\nabla_S \cdot \mathbf{v}, p) - \eta \rho \|\nabla_S \mathbf{v}\|^2 - \frac{\sigma \rho}{\epsilon Pe} \|\nabla_S \mu\|^2 - \frac{\rho \sigma}{\epsilon} ((\mathbf{v}\phi, \nabla_S \mu) + (\mu, \nabla_S \cdot (\phi \mathbf{v})))$$

$$= -\eta \rho \|\nabla_S \mathbf{v}\|^2 - \frac{\sigma \rho}{\epsilon Pe} \|\nabla_S \mu\|^2 \leq 0. \tag{3}$$

3. Numerical approximations

3.1. Second-order spatial accurate operators on surfaces

Let us introduce the discretization of gradient, divergence and Laplace–Beltrami operators defined on triangular surface mesh $\Sigma := (P, T)$, where $P = \{\mathbf{p}_i | 1 \leq i \leq N_P\}$ is the set of vertices and $T = \{T_i | 1 \leq i \leq N_T\}$ is the set of triangles. Here, N_P and N_T are the number of vertices and triangles, respectively. For $j = 0, 1, \ldots, s$, let $\mathbf{p}_j$ be counterclockwise relative to the outside of the polygon and satisfy $\mathbf{p}_s = \mathbf{p}_0$. Let us define triangle T_j with three vertices $\mathbf{p}$, $\mathbf{p}_j$ and $\mathbf{p}_{j+1}$, where $G_i = (\mathbf{p} + \mathbf{p}_j + \mathbf{p}_{j+1})/3$ is the centroid of this triangle as the blue triangle in Fig. 1. The normal vector $\mathbf{N}(\mathbf{p})$ at $\mathbf{p} \in P$ can be denoted as

$$\mathbf{N}(\mathbf{p}) = \sum_{j=0}^{p-1} \omega_j \mathbf{N}_j / \left\| \sum_{j=0}^{p-1} \omega_j \mathbf{N}_j \right\| \tag{4}$$

where $\mathbf{N}_j$ is the unit normal vector to T_j and $\omega_j = \|\mathbf{G}_j - \mathbf{p}\|^{-2} / \sum_{k=0}^{s-1} \|\mathbf{G}_k - \mathbf{p}\|^{-2}$. Then the outer normal vector $\mathbf{n}_p(\mathbf{G}_j)$ at $\mathbf{G}_j$ can be denoted as

$$\mathbf{n}_p(\mathbf{G}_j) = \frac{(\mathbf{G}_{j+1} - \mathbf{G}_j) \times \mathbf{N}_j}{\|(\mathbf{G}_{j+1} - \mathbf{G}_j) \times \mathbf{N}_j\|} \text{ and } \mathbf{n}_p(\mathbf{G}_{j+1}) = \frac{(\mathbf{G}_{j+1} - \mathbf{G}_j) \times \mathbf{N}_{j+1}}{\|(\mathbf{G}_{j+1} - \mathbf{G}_j) \times \mathbf{N}_{j+1}\|}. \tag{5}$$
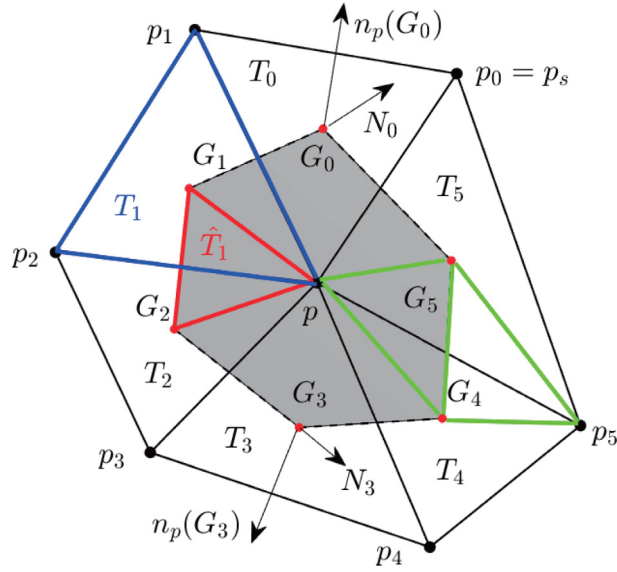
Fig. 1. Schematic illustration of the vertex **p** and its neighbors for evaluating the gradient, divergence and Laplace–Beltrami operators. (For interpretation of the references to color in this figure legend, the reader is referred to the web version of this article.)

In the following discussion, we will use ∇_h, $\nabla_h\cdot$ and Δ_h to denote the discrete gradient, divergence and Laplace–Beltrami operators, respectively. To obtain second order accuracy discrete operators, let us start with a Taylor expansion,

$$
\begin{cases}
\mathbf{X}(\mathbf{p}) - \mathbf{X}(\mathbf{G}_j) = \langle \nabla_h \mathbf{X}(\mathbf{G}_j), \mathbf{p} - \mathbf{G}_j \rangle + 0.5\Delta_h \mathbf{X}(\mathbf{G}_j) \|\mathbf{p} - \mathbf{G}_j\|^2, \\
\mathbf{X}(\mathbf{p}_j) - \mathbf{X}(\mathbf{G}_j) = \langle \nabla_h \mathbf{X}(\mathbf{G}_j), \mathbf{p}_j - \mathbf{G}_j \rangle + 0.5\Delta_h \mathbf{X}(\mathbf{G}_j) \|\mathbf{p}_j - \mathbf{G}_j\|^2, \\
\mathbf{X}(\mathbf{p}_{j+1}) - \mathbf{X}(\mathbf{G}_j) = \langle \nabla_h \mathbf{X}(\mathbf{G}_j), \mathbf{p}_{j+1} - \mathbf{G}_j \rangle + 0.5\Delta_h \mathbf{X}(\mathbf{G}_j) \|\mathbf{p}_{j+1} - \mathbf{G}_j\|^2,
\end{cases}
\tag{6}
$$

where $\nabla_h \mathbf{X}(\mathbf{G}_j)$ and $\Delta_h \mathbf{X}(\mathbf{G}_j)$ are the approximate surface gradient and surface Laplacian of $\mathbf{X}(\mathbf{G}_j)$ at the centroid $\mathbf{G}_j$. It is obviously that $\nabla_h \mathbf{X}(\mathbf{G}_j)$, $\mathbf{p}_j - \mathbf{G}_j$, and $\mathbf{p}_{j+1} - \mathbf{G}_j$ are in the same triangle plane, we can assume that $\nabla_h \mathbf{X}(\mathbf{G}_j)$ takes the following form

$$
\nabla_h \mathbf{X}(\mathbf{G}_j) = \alpha_j(\mathbf{p}_j - \mathbf{G}_j) + \beta_j(\mathbf{p}_{j+1} - \mathbf{G}_j),
\tag{7}
$$

where α_j and β_j are constants. Combining Eqs. (6) and (7), the coefficients of the discrete gradient operator can be computed by

$$
\begin{pmatrix}
\alpha_j \\
\beta_j \\
0.5\Delta_h \mathbf{X}(\mathbf{G}_j)
\end{pmatrix}
= B_j^{-1}
\begin{pmatrix}
\mathbf{X}(\mathbf{p}) - \mathbf{X}(\mathbf{G}_j) \\
\mathbf{X}(\mathbf{p}_j) - \mathbf{X}(\mathbf{G}_j) \\
\mathbf{X}(\mathbf{p}_{j+1}) - \mathbf{X}(\mathbf{G}_j)
\end{pmatrix},
\tag{8}
$$

where $B_j = \begin{pmatrix}
\langle \mathbf{p}_j - \mathbf{G}_j, \mathbf{p} - \mathbf{G}_j \rangle & \langle \mathbf{p}_{j+1} - \mathbf{G}_j, \mathbf{p} - \mathbf{G}_j \rangle & \|\mathbf{p} - \mathbf{G}_j\|^2 \\
\langle \mathbf{p}_j - \mathbf{G}_j, \mathbf{p}_j - \mathbf{G}_j \rangle & \langle \mathbf{p}_{j+1} - \mathbf{G}_j, \mathbf{p}_j - \mathbf{G}_j \rangle & \|\mathbf{p}_j - \mathbf{G}_j\|^2 \\
\langle \mathbf{p}_j - \mathbf{G}_j, \mathbf{p}_{j+1} - \mathbf{G}_j \rangle & \langle \mathbf{p}_{j+1} - \mathbf{G}_j, \mathbf{p}_{j+1} - \mathbf{G}_j \rangle & \|\mathbf{p}_{j+1} - \mathbf{G}_j\|^2
\end{pmatrix}.$ (9)

After calculating α_j and β_j and substituting the results into Eq. (7), we can compute $\nabla_h \mathbf{X}(\mathbf{G}_j)$. Note that it is not difficult to prove that matrix B_j has full rank, which implies B_j^{-1} exists. In addition, we can prove that $\Delta_h \mathbf{X}(\mathbf{G}_j)$

equals zero because of

$$
\begin{aligned}
\Delta_h \mathbf{X}\left(\mathbf{G}_j\right) = &\frac{2}{\left|B_j\right|} \cdot \Big(\big(\langle \mathbf{p}_j - \mathbf{G}_j, \mathbf{p}_j - \mathbf{G}_j \rangle \cdot \langle \mathbf{p}_{j+1} - \mathbf{G}_j, \mathbf{p}_{j+1} - \mathbf{G}_j \rangle \\
&- \langle \mathbf{p}_{j+1} - \mathbf{G}_j, \mathbf{p}_j - \mathbf{G}_j \rangle \cdot \langle \mathbf{p}_j - \mathbf{G}_j, \mathbf{p}_{j+1} - \mathbf{G}_j \rangle \big) \\
&- \big(\langle \mathbf{p}_j - \mathbf{G}_j, \mathbf{p} - \mathbf{G}_j \rangle \cdot \langle \mathbf{p}_{j+1} - \mathbf{G}_j, \mathbf{p}_{j+1} - \mathbf{G}_j \rangle \\
&- \langle \mathbf{p}_j - \mathbf{G}_j, \mathbf{p}_{j+1} - \mathbf{G}_j \rangle \cdot \langle \mathbf{p}_{j+1} - \mathbf{G}_j, \mathbf{p} - \mathbf{G}_j \rangle \big) \\
&+ \big(\langle \mathbf{p}_j - \mathbf{G}_j, \mathbf{p} - \mathbf{G}_j \rangle \cdot \langle \mathbf{p}_{j+1} - \mathbf{G}_j, \mathbf{p}_j - \mathbf{G}_j \rangle \\
&- \langle \mathbf{p}_j - \mathbf{G}_j, \mathbf{p}_j - \mathbf{G}_j \rangle \cdot \langle \mathbf{p}_{j+1} - \mathbf{G}_j, \mathbf{p} - \mathbf{G}_j \rangle \big) \Big) = 0.
\end{aligned}
$$

Thus, by combining Eqs. (7)–(9), we confirm that $\nabla_h \mathbf{X}(\mathbf{G}_j)$ has second-order accuracy in space. Based on the Green's formula, we can easily obtain

$$
\begin{aligned}
\int_{\mathcal{S}} \Delta \mathbf{X}(\mathbf{p}) d\mathbf{s} &= \int_{\partial \mathcal{S}} \langle \nabla \mathbf{X}(\mathbf{p}), \mathbf{n} \rangle da \\
&\approx \sum_{j=0}^{s-1} \left(\left\| \mathbf{G}_{j+1} - \mathbf{G}_j \right\| \right) \int_0^1 \left\langle q \nabla_h \mathbf{X}\left(\mathbf{G}_j\right) + (1-q) \nabla_h \mathbf{X}\left(\mathbf{G}_{j+1}\right), q \mathbf{n}\left(\mathbf{G}_j\right) + (1-q) \mathbf{n}\left(\mathbf{G}_{j+1}\right) \right\rangle dq \\
&= \sum_{j=0}^{s-1} \frac{\left\| \mathbf{G}_{j+1} - \mathbf{G}_j \right\|}{6} \left(2 \left\langle \nabla_h \mathbf{X}\left(\mathbf{G}_j\right), \mathbf{n}\left(\mathbf{G}_j\right) \right\rangle + 2 \left\langle \nabla_h \mathbf{X}\left(\mathbf{G}_{j+1}\right), \mathbf{n}\left(\mathbf{G}_{j+1}\right) \right\rangle \right. \\
&\qquad\qquad\qquad\qquad\qquad \left. + \left\langle \nabla_h \mathbf{X}\left(\mathbf{G}_j\right), \mathbf{n}\left(\mathbf{G}_{j+1}\right) \right\rangle + \left\langle \nabla_h \mathbf{X}\left(\mathbf{G}_{j+1}\right), \mathbf{n}\left(\mathbf{G}_j\right) \right\rangle \right),
\end{aligned} \tag{10}
$$

where $\mathbf{n}$ is the outer normal vector of the S. Thus, we can derive the approximate Laplace–Beltrami operator as

$$
\begin{aligned}
\Delta_h \mathbf{X}(\mathbf{p}) = \frac{1}{A(\mathbf{p})} \sum_{j=0}^{s-1} \frac{\|\mathbf{G}_{j+1} - \mathbf{G}_j\|}{6} \big(& 2 \left\langle \nabla_h \mathbf{X}(\mathbf{G}_j), \ \mathbf{n}(\mathbf{G}_j) \right\rangle + 2 \left\langle \nabla_h \mathbf{X}(\mathbf{G}_{j+1}), \ \mathbf{n}(\mathbf{G}_{j+1}) \right\rangle \\
& + \left\langle \nabla_h \mathbf{X}(\mathbf{G}_j), \ \mathbf{n}(\mathbf{G}_{j+1}) \right\rangle + \left\langle \nabla_h \mathbf{X}(\mathbf{G}_{j+1}), \ \mathbf{n}(\mathbf{G}_j) \right\rangle \big),
\end{aligned} \tag{11}
$$

where $A(\mathbf{p})$ is the area of polygon around by $G_j (j = 0, \ldots, s-1)$ as shown in the shadow part of Fig. 1. $A(\mathbf{p})$ can be computed as $A(\mathbf{p}) = \sum_{j=0}^{s-1} \left| \hat{T}_j \right|$. Here $\left| \hat{T}_j \right|$ is the area of the triangle $\hat{T}_j$ with $\mathbf{p}$, $\mathbf{G}_j$ and $\mathbf{G}_{j+1}$, which are remarked by the red triangle in Fig. 1. The definition of the Laplace–Beltrami operator in Eq. (11), requires the gradient of $\mathbf{X}(\mathbf{G}_j)$ at the centroid $\mathbf{G}_j$ of each triangle, i.e. $\nabla_h \mathbf{X}(\mathbf{G}_j)$, which has been proved to be second-order in Eq. (7). Therefore, it is easy to prove that the discrete Laplace–Beltrami operator has second-order accuracy in space. Then the discrete divergence $\nabla_h \cdot \mathbf{X}$ can be derived from Green's formula in the same way as

$$
\begin{aligned}
\nabla_h \cdot \mathbf{X}(\mathbf{p}) = \frac{1}{A(\mathbf{p})} \sum_{j=0}^{s-1} \frac{\|\mathbf{G}_{j+1} - \mathbf{G}_j\|}{6} \big(& 2 \left\langle \mathbf{X}\left(\mathbf{G}_j\right), \mathbf{n}\left(\mathbf{G}_j\right) \right\rangle + 2 \left\langle \mathbf{X}\left(\mathbf{G}_{j+1}\right), \mathbf{n}\left(\mathbf{G}_{j+1}\right) \right\rangle \\
& + \left\langle \mathbf{X}\left(\mathbf{G}_j\right), \mathbf{n}\left(\mathbf{G}_{j+1}\right) \right\rangle + \left\langle \mathbf{X}\left(\mathbf{G}_{j+1}\right), \mathbf{n}\left(\mathbf{G}_j\right) \right\rangle \big),
\end{aligned} \tag{12}
$$

Finally, let us consider the gradient of $\mathbf{X}$ at vertex $\mathbf{p}$, i.e. $\nabla_h \mathbf{X}(\mathbf{p})$. Starting from the following Taylor expansion:

$$
\mathbf{X}(\mathbf{G}_j) - \mathbf{X}(\mathbf{p}) = \left\langle \nabla_h \mathbf{X}(\mathbf{p}), \mathbf{G}_j - \mathbf{p} \right\rangle + 0.5 \Delta_h \mathbf{X}(\mathbf{p}) \|\mathbf{G}_j - \mathbf{p}\|^2, \tag{13}
$$

where $\Delta_h \mathbf{X}(\mathbf{p})$ can be computed as Eq. (11) with second-order accuracy. Combining the first equation of system (6) with Eq. (13), we obtain

$$
\left\langle \nabla_h \mathbf{X}(\mathbf{p}), \mathbf{G}_j - \mathbf{p} \right\rangle = \left\langle \nabla_h \mathbf{X}(\mathbf{G}_j), \mathbf{G}_j - \mathbf{p} \right\rangle - 0.5 \Delta_h \mathbf{X}(\mathbf{p}) \|\mathbf{G}_j - \mathbf{p}\|^2. \tag{14}
$$

Let us define

$$
\nabla_h \mathbf{X}(\mathbf{p}) = \nabla_h \mathbf{X}(\mathbf{G}_j) - 0.5 \Delta_h \mathbf{X}(\mathbf{p})(\mathbf{G}_j - \mathbf{p}). \tag{15}
$$

By multiplying the weight constant ω_j to Eq. (15) and adding these results, we can obtain

$$\nabla_h \mathbf{X}(\mathbf{p}) = \sum_{j=0}^{s-1} \omega_j \nabla_h \mathbf{X}(\mathbf{G}_j) - \sum_{j=0}^{s-1} \frac{\omega_j}{2} \Delta_h \mathbf{X}(\mathbf{p})(\mathbf{G}_j - \mathbf{p}), \tag{16}$$

where $\omega_j = \left\| \mathbf{G}_j - \mathbf{p} \right\|^{-2} / \sum_{k=0}^{s-1} \| \mathbf{G}_k - \mathbf{p} \|^{-2}$. Note that Eqs. (15) and (16) have second order accuracy in spatial space. We will use Eq. (16) to discretize the gradient operator. Herein, the discrete gradient(∇_h), divergence($\nabla_h \cdot$) and Laplacian–Beltrami (Δ_h) operators have been defined with second-order spatial accuracy.

3.2. Second-order temporal accuracy scheme for CHNS

Let us define $\mathbf{v}_i^n$ and ϕ_i^n be the approximation of $\mathbf{v}(\mathbf{p}_i, n\Delta t)$ and $\phi(\mathbf{p}_i, n\Delta t)$ at vertex $\mathbf{p}_i$, where $\Delta t = T/N_t$ is the time step, T is the final time and N_t is the total number of time steps. For the given initial condition ϕ_i^0 and $\mathbf{v}_i^0$, we assume that the first time level solution satisfies $\phi_i^{-1} = \phi_i^0$ and $\mathbf{v}_i^{-1} = \mathbf{v}_i^0$. For obtaining a second-order numerical solution, we apply a Crank–Nicolson-type method under the projection framework for the CHNS scheme as follows:

$$\frac{\phi_i^{n+1} - \phi_i^n}{\Delta t} + \nabla_h \cdot (\tilde{\phi}_i^{n+\frac{1}{2}}(\frac{1}{2}\hat{\mathbf{v}}_i^{n+1} + \frac{1}{2}\mathbf{v}_i^n)) = \frac{1}{Pe} \Delta_h \mu_i^{n+\frac{1}{2}}, \tag{17a}$$

$$\mu_i^{n+\frac{1}{2}} = \frac{f(\phi_i^{n+1}) - f(\phi_i^n)}{\phi_i^{n+1} - \phi_i^n} - \epsilon^2 \Delta_h \frac{\phi_i^{n+1} + \phi_i^n}{2}, \tag{17b}$$

$$\rho \frac{\hat{\mathbf{v}}_i^{n+1} - \mathbf{v}_i^n}{\Delta t} + \frac{\rho}{2}\left(\tilde{\mathbf{v}}_i^{n+\frac{1}{2}} \cdot \nabla_h(\frac{1}{2}\hat{\mathbf{v}}_i^{n+1} + \frac{1}{2}\mathbf{v}_i^n) + \nabla_h \cdot \left(\tilde{\mathbf{v}}_i^{n+\frac{1}{2}} \otimes (\frac{1}{2}\hat{\mathbf{v}}_i^{n+1} + \frac{1}{2}\mathbf{v}_i^n) \right) \right)$$
$$= -\nabla_h p_i^n + \nabla_h \cdot \left(\eta \nabla_h(\frac{1}{2}\hat{\mathbf{v}}_i^{n+1} + \frac{1}{2}\mathbf{v}_i^n) \right) - \frac{\sigma}{\epsilon} \tilde{\phi}_i^{n+\frac{1}{2}} \nabla_h \mu_i^{n+\frac{1}{2}} \tag{17c}$$

$$\rho \frac{\mathbf{v}_i^{n+1} - \hat{\mathbf{v}}_i^{n+1}}{\Delta t} + \frac{1}{2}\nabla_h \left(p_i^{n+1} - p_i^n \right) = 0, \tag{17d}$$

$$\nabla_h \cdot \mathbf{v}_i^{n+1} = 0, \tag{17e}$$

where $\tilde{(\cdot)}^{n+\frac{1}{2}} = \left(3(\cdot)^n - (\cdot)^{n-1}\right)/2$ and $(\cdot)^{n+\frac{1}{2}} = \left((\cdot)^{n+1} + (\cdot)^n\right)/2$. We use $\hat{\mathbf{v}}_i$ to denote the intermediate velocity of the projection method. Before we proceed, we must define inner products over the curved surfaces for deriving the proposed numerical schemes. Here let us define ϕ_i and ψ_i as the functions on surfaces $\phi_i := \phi(\mathbf{p}_i)$ and $\psi_i := \psi(\mathbf{p}_i)$, respectively. We define the discrete inner product at the vertex by $(\phi, \psi)_h := \sum_{\mathbf{p}_i \in P} \phi_i \psi_i A(\mathbf{p}_i)$, and $(\nabla_h \phi, \nabla_h \psi)_h = \sum_{\mathbf{p}_i \in P} \left(A(\mathbf{p}_i) \sum_{j=0}^{s-1} \nabla_h \phi(\mathbf{G}_j) \cdot \nabla_h \psi(\mathbf{G}_j) \right)$, thus the discrete norm can be defined as $\|\phi\|_h^2 = (\phi, \phi)_h$ and $\|\nabla_h \phi\|_h^2 = (\nabla_h \phi, \nabla_h \phi)_h$, respectively.

In the following section, we will show the unconditional stability of our proposed scheme Eqs. (17), which is a discrete representation of Eq. (3). After that, we prove the mass conservation law with the discrete schemes.

Theorem 1. *The solutions of Eqs. (17) make the energy decay with respect to time, i.e.*

$$\left(E^{n+1} + \Delta t^2 \|\nabla_h p^{n+1}\|_h^2/(8\rho)\right) - \left(E^n + \Delta t^2 \|\nabla_h p^n\|_h^2/(8\rho)\right)$$
$$= -\Delta t \eta \|\nabla_h \hat{\mathbf{v}}^{n+\frac{1}{2}}\|_h^2 - \frac{\rho \Delta t \sigma}{\epsilon Pe} \|\nabla_h \mu^{n+\frac{1}{2}}\|_h^2 \leq 0, \tag{18}$$

where $E^n = \rho \|\mathbf{v}^n\|_h^2/2 + \rho\epsilon\sigma \|\nabla_h \phi^n\|_h^2/2 + \rho\sigma \left(f(\phi^n), 1\right)_h /\epsilon$ is the total energy.

Proof. Let us denote $\phi_t^{n+\frac{1}{2}} = (\phi^{n+1} - \phi^n)/\Delta t$. By multiplying Eq. (17a) with $\mu^{n+\frac{1}{2}}$, we obtain

$$\left(\mu^{n+\frac{1}{2}}, \phi_t^{n+\frac{1}{2}}\right)_h = -\|\nabla_h \mu^{n+\frac{1}{2}}\|_h^2/Pe - \left(\mu^{n+\frac{1}{2}}, \nabla_h \cdot \left(\tilde{\phi}^{n+\frac{1}{2}} \hat{\mathbf{v}}^{n+\frac{1}{2}}\right)\right)_h. \tag{19}$$

Taking the L_2 inner product of Eq. (17c) with $\hat{\mathbf{v}}^{n+\frac{1}{2}} \Delta t / \rho$, we have

$$\frac{\left(\left\|\hat{\mathbf{v}}^{n+1}\right\|_h^2 - \|\mathbf{v}^n\|_h^2\right)}{2\Delta t} = -\frac{1}{\rho}\left(\nabla_h p^n, \hat{\mathbf{v}}^{n+\frac{1}{2}}\right)_h - \frac{\sigma}{\epsilon}\left(\tilde{\phi}^{n+\frac{1}{2}}\nabla_h \mu^{n+\frac{1}{2}}, \hat{\mathbf{v}}^{n+\frac{1}{2}}\right)_h - \frac{\eta}{\rho}\left\|\nabla_h \hat{\mathbf{v}}^{n+\frac{1}{2}}\right\|_h^2. \tag{20}$$

Note that

$$\begin{aligned}
&\left(\hat{\mathbf{v}}^{n+\frac{1}{2}}, \tilde{\mathbf{v}}^{n+\frac{1}{2}} \cdot \nabla_h \hat{\mathbf{v}}^{n+\frac{1}{2}} + \nabla_h \cdot \left(\tilde{\mathbf{v}}^{n+\frac{1}{2}}\hat{\mathbf{v}}^{n+\frac{1}{2}}\right)\right)_h \\
&= \left(\hat{\mathbf{v}}^{n+\frac{1}{2}}\tilde{\mathbf{v}}^{n+\frac{1}{2}}, \nabla_h \hat{\mathbf{v}}^{n+\frac{1}{2}}\right)_h + \left(\hat{\mathbf{v}}^{n+\frac{1}{2}}, \nabla_h \cdot \left(\tilde{\mathbf{v}}^{n+\frac{1}{2}}\hat{\mathbf{v}}^{n+\frac{1}{2}}\right)\right)_h = 0
\end{aligned} \tag{21}$$

during the computation of Eq. (20). Taking the L_2 inner product of Eq. (17d) with $\mathbf{v}^{n+1}\Delta t/\rho$, we have

$$\left(\mathbf{v}^{n+1}, \mathbf{v}^{n+1} - \hat{\mathbf{v}}^{n+1}\right)_h = \left(-\Delta t/(2\rho)\nabla_h(p^{n+1} - p^n), \mathbf{v}^{n+1}\right)_h = \left(\Delta t/(2\rho)(p^{n+1} - p^n), \nabla_h \cdot \mathbf{v}^{n+1}\right)_h = 0,$$

from which we can derive the following equation:

$$\frac{1}{2}\left(\left\|\mathbf{v}^{n+1}\right\|_h^2 - \left\|\hat{\mathbf{v}}^{n+1}\right\|_h^2\right) = -\frac{1}{2}\left\|\mathbf{v}^{n+1} - \hat{\mathbf{v}}^{n+1}\right\|_h^2 = -\frac{\Delta t^2}{8\rho^2}\left\|\nabla_h\left(p^{n+1} - p^n\right)\right\|_h^2. \tag{22}$$

Rewriting the projection step of Eq. (17d) as

$$\frac{\mathbf{v}^{n+1} + \mathbf{v}^n - 2\hat{\mathbf{v}}^{n+\frac{1}{2}}}{\Delta t} + \frac{1}{2\rho}\nabla_h\left(p^{n+1} - p^n\right) = 0, \tag{23}$$

which leads to

$$\frac{\Delta t^2}{8}\left\|\nabla_h\left(p^{n+1} - p^n\right)\right\|_h^2 = \frac{\Delta t^2}{8}\left(\left\|\nabla_h p^{n+1}\right\|_h^2 - \left\|\nabla_h p^n\right\|_h^2\right) - \rho\Delta t\left(\nabla_h p^n, \hat{\mathbf{v}}^{n+\frac{1}{2}}\right)_h, \tag{24}$$

by taking the inner product with $\Delta t^2\nabla_h p^n/2$. Finally, multiplying Eqs. (20) and (22) by $1/\Delta t$ and summing up the results with $\Delta t\left(\|\nabla_h p^{n+1}\|_h^2 - \|\nabla_h p^n\|_h^2\right)/8$ and $\left(\mu^{n+\frac{1}{2}}, \phi_t^{n+\frac{1}{2}}\right)_h$, the energy dissipation with the discrete form can be proved as follows:

$$\begin{aligned}
&\left(E^{n+1} + \Delta t^2\|\nabla_h p^{n+1}\|_h^2/(8\rho)\right) - \left(E^n + \Delta t^2\|\nabla_h p^n\|_h^2/(8\rho)\right) \\
&= \frac{\rho(\|\mathbf{v}^{n+1}\|_h^2 - \|\mathbf{v}^n\|_h^2)}{2} + \Delta t\rho\sigma\epsilon\left(\nabla_h \phi^{n+\frac{1}{2}}, \nabla_h \phi_t^{n+\frac{1}{2}}\right)_h \\
&\quad + \frac{\Delta t\rho\sigma}{\epsilon}\left(\frac{f(\phi^{n+1}) - f(\phi^n)}{\phi^{n+1} - \phi^n}, \phi_t^{n+\frac{1}{2}}\right)_h + \frac{\Delta t^2}{8\rho}\left(\|\nabla_h p^{n+1}\|_h^2 - \|\nabla_h p^n\|_h^2\right) \\
&= \frac{\rho(\|\mathbf{v}^{n+1}\|_h^2 - \|\mathbf{v}^n\|_h^2)}{2} - \Delta t\rho\sigma\epsilon(\Delta_h \phi^{n+\frac{1}{2}}, \phi_t^{n+\frac{1}{2}})_h \\
&\quad + \frac{\Delta t\rho\sigma}{\epsilon}\left(\frac{f(\phi^{n+1}) - f(\phi^n)}{\phi^{n+1} - \phi^n}, \phi_t^{n+\frac{1}{2}}\right)_h + \frac{\Delta t^2}{8\rho}\left(\|\nabla_h p^{n+1}\|_h^2 - \|\nabla_h p^n\|_h^2\right) \\
&= \frac{\rho(\|\mathbf{v}^{n+1}\|_h^2 - \|\hat{\mathbf{v}}^{n+1}\|_h^2)}{2} + \frac{\rho(\|\hat{\mathbf{v}}^{n+1}\|_h^2 - \|\mathbf{v}^n\|_h^2)}{2} \\
&\quad + \frac{\Delta t\rho\sigma}{\epsilon}\left(\mu^{n+\frac{1}{2}}, \phi_t^{n+\frac{1}{2}}\right)_h + \frac{\Delta t^2}{8\rho}\left(\|\nabla_h p^{n+1}\|_h^2 - \|\nabla_h p^n\|_h^2\right) \\
&= -\Delta t\eta\|\nabla_h \hat{\mathbf{v}}^{n+\frac{1}{2}}\|_h^2 + \frac{\rho\sigma\Delta t}{\epsilon}\left(-\frac{\|\nabla_h \mu^{n+\frac{1}{2}}\|}{Pe} - \left(\mu^{n+\frac{1}{2}}, \nabla_h \cdot \left(\tilde{\phi}^{n+\frac{1}{2}}\hat{\mathbf{v}}^{n+\frac{1}{2}}\right)\right)\right) \\
&\quad - \frac{\Delta t\sigma\rho}{\epsilon}\left(\tilde{\phi}^{n+\frac{1}{2}}\nabla_h \mu^{n+\frac{1}{2}}, \hat{\mathbf{v}}^{n+\frac{1}{2}}\right) \\
&= -\Delta t\eta\|\nabla_h \hat{\mathbf{v}}^{n+\frac{1}{2}}\|_h^2 - \frac{\Delta t\rho\sigma}{\epsilon Pe}\|\nabla_h \mu^{n+\frac{1}{2}}\|_h^2 \leq 0,
\end{aligned}$$

which corresponds to Eq. (18). $\square$

It is worth pointing that the modified energy $E^n + \Delta t^2 \|\nabla_h p^n\|^2/(8\rho)$ is non-increasing in time. Although we cannot prove that the original energy is unconditionally decreasing, we can see that the original energy is less than the modified energy, i.e., $E^n \le E^n + \Delta t^2 \|\nabla_h p^1\|^2/(8\rho)$. Therefore, the discrete original energy is bounded and maybe be decreasing in time. Later, we consider the mass conservation of our proposed discrete scheme.

Theorem 2. *The proposed numerical scheme Eq.* (17) *satisfies the total mass conservation property, i.e.*

$$\sum_{\mathbf{p}_i \in P} \phi_i^{n+1} A(\mathbf{p}_i) = \sum_{\mathbf{p}_i \in P} \phi_i^n A(\mathbf{p}_i). \tag{25}$$

Proof. Multiplying $\sum_{\mathbf{p}_i \in P} \phi_i^{n+1}$ and $\sum_{\mathbf{p}_i \in P} \phi_i^n$ with $A(\mathbf{p})$ and summing by parts, we can obtain

$$
\begin{aligned}
&\sum_{\mathbf{p}_i \in P} \phi_i^{n+1} A(\mathbf{p}_i) - \sum_{\mathbf{p}_i \in P} \phi_i^n A(\mathbf{p}_i) \\
&= \Delta t \sum_{\mathbf{p}_i \in P} \left(\frac{\Delta_h \mu_i^{n+\frac{1}{2}}}{Pe} + \nabla_h \cdot (\tilde{\phi}_i^{n+\frac{1}{2}} \hat{\mathbf{v}}_i^{n+\frac{1}{2}}) \right) A(\mathbf{p}_i) \\
&= \Delta t \sum_{\mathbf{p}_i \in P} \left(\sum_{j=0}^{s-1} \frac{\|\mathbf{G}_{j+1} - \mathbf{G}_j\|}{6} \left(2 \left\langle \left(\frac{\nabla_h \mu^{n+\frac{1}{2}}}{Pe} + \tilde{\phi}^{n+\frac{1}{2}} \hat{\mathbf{v}}^{n+\frac{1}{2}} \right)(\mathbf{G}_j), \ \mathbf{n}(\mathbf{G}_j) \right\rangle \right. \right. \\
&\quad + 2 \left\langle \left(\frac{\nabla_h \mu^{n+\frac{1}{2}}}{Pe} + \tilde{\phi}^{n+\frac{1}{2}} \hat{\mathbf{v}}^{n+\frac{1}{2}} \right)(\mathbf{G}_{j+1}), \ \mathbf{n}(\mathbf{G}_{j+1}) \right\rangle + \left\langle \left(\frac{\nabla_h \mu^{n+\frac{1}{2}}}{Pe} + \tilde{\phi}^{n+\frac{1}{2}} \hat{\mathbf{v}}^{n+\frac{1}{2}} \right)(\mathbf{G}_j), \ \mathbf{n}(\mathbf{G}_{j+1}) \right\rangle \\
&\quad \left. \left. + \left\langle \left(\frac{\nabla_h \mu^{n+\frac{1}{2}}}{Pe} + \tilde{\phi}^{n+\frac{1}{2}} \hat{\mathbf{v}}^{n+\frac{1}{2}} \right)(\mathbf{G}_{j+1}), \ \mathbf{n}(\mathbf{G}_j) \right\rangle \right) \right).
\end{aligned} \tag{26}
$$

Let us denote the edge of $\mathbf{G}_j \mathbf{G}_{j+1} \in \tilde{P}$ as $\overline{\mathbf{G}_j \mathbf{G}_{j+1}}$ as the green triangles in Fig. 1. Thus, Eq. (26) can be recalculated with respect to the edges over the dual mesh $\tilde{P}$ as

$$
\begin{aligned}
&\sum_{\mathbf{p}_i \in P} \phi_i^{n+1} A(\mathbf{p}_i) - \sum_{\mathbf{p}_i \in P} \phi_i^n A(\mathbf{p}_i) \\
&= \Delta t \sum_{\overline{\mathbf{G}_j \mathbf{G}_{j+1}} \in \tilde{P}} \left(\frac{\|\mathbf{G}_{j+1} - \mathbf{G}_j\|}{6} \left(2 \left\langle \left(\frac{\nabla_h \mu^{n+\frac{1}{2}}}{Pe} + \tilde{\phi}^{n+\frac{1}{2}} \hat{\mathbf{v}}^{n+\frac{1}{2}} \right)(\mathbf{G}_j), \ \mathbf{n}_\mathbf{p}(\mathbf{G}_j) \right\rangle \right. \right. \\
&\quad + 2 \left\langle \left(\frac{\nabla_h \mu^{n+\frac{1}{2}}}{Pe} + \tilde{\phi}^{n+\frac{1}{2}} \hat{\mathbf{v}}^{n+\frac{1}{2}} \right)(\mathbf{G}_{j+1}), \ \mathbf{n}_\mathbf{p}(\mathbf{G}_{j+1}) \right\rangle + \left\langle \left(\frac{\nabla_h \mu^{n+\frac{1}{2}}}{Pe} + \tilde{\phi}^{n+\frac{1}{2}} \hat{\mathbf{v}}^{n+\frac{1}{2}} \right)(\mathbf{G}_j), \ \mathbf{n}_\mathbf{p}(\mathbf{G}_{j+1}) \right\rangle \\
&\quad + \left\langle \left(\frac{\nabla_h \mu^{n+\frac{1}{2}}}{Pe} + \tilde{\phi}^{n+\frac{1}{2}} \hat{\mathbf{v}}^{n+\frac{1}{2}} \right)(\mathbf{G}_{j+1}), \ \mathbf{n}_\mathbf{p}(\mathbf{G}_j) \right\rangle + 2 \left\langle \left(\frac{\nabla_h \mu^{n+\frac{1}{2}}}{Pe} + \tilde{\phi}^{n+\frac{1}{2}} \hat{\mathbf{v}}^{n+\frac{1}{2}} \right)(\mathbf{G}_j), \ \mathbf{n}_{\mathbf{p}_{j+1}}(\mathbf{G}_j) \right\rangle \\
&\quad + 2 \left\langle \left(\frac{\nabla_h \mu^{n+\frac{1}{2}}}{Pe} + \tilde{\phi}^{n+\frac{1}{2}} \hat{\mathbf{v}}^{n+\frac{1}{2}} \right)(\mathbf{G}_{j+1}), \ \mathbf{n}_{\mathbf{p}_{j+1}}(\mathbf{G}_{j+1}) \right\rangle \\
&\quad + \left\langle \left(\frac{\nabla_h \mu^{n+\frac{1}{2}}}{Pe} + \tilde{\phi}^{n+\frac{1}{2}} \hat{\mathbf{v}}^{n+\frac{1}{2}} \right)(\mathbf{G}_j), \ \mathbf{n}_{\mathbf{p}_{j+1}}(\mathbf{G}_{j+1}) \right\rangle \\
&\quad \left. \left. + \left\langle \left(\frac{\nabla_h \mu^{n+\frac{1}{2}}}{Pe} + \tilde{\phi}^{n+\frac{1}{2}} \hat{\mathbf{v}}^{n+\frac{1}{2}} \right)(\mathbf{G}_{j+1}), \ \mathbf{n}_{\mathbf{p}_{j+1}}(\mathbf{G}_j) \right\rangle \right) \right).
\end{aligned} \tag{27}
$$

Since the vertices are labeled counterclockwise, the normal vectors $\mathbf{n}_{\mathbf{p}_{j+1}}(\mathbf{G}_j)$ and $\mathbf{n}_{\mathbf{p}_{j+1}}(\mathbf{G}_{j+1})$ can be recalculated as

$$
\begin{cases}
\mathbf{n}_{\mathbf{p}_{j+1}}(\mathbf{G}_j) = \dfrac{(\mathbf{G}_j - \mathbf{G}_{j+1}) \times \mathbf{N}_j}{\|(\mathbf{G}_j - \mathbf{G}_{j+1}) \times \mathbf{N}_j\|} = -\mathbf{n}_{\mathbf{p}}(\mathbf{G}_j), \\[4mm]
\mathbf{n}_{\mathbf{p}_{j+1}}(\mathbf{G}_{j+1}) = \dfrac{(\mathbf{G}_j - \mathbf{G}_{j+1}) \times \mathbf{N}_{j+1}}{\|(\mathbf{G}_j - \mathbf{G}_{j+1}) \times \mathbf{N}_{j+1}\|} = -\mathbf{n}_{\mathbf{p}}(\mathbf{G}_{j+1}).
\end{cases}
\tag{28}
$$

By combining Eqs. (26)–(28), we complete the proof. $\square$

Theorem 3. *Let $\Sigma := (P, T)$ be the triangular mesh without boundary and denote ϕ and ψ to be the vector field on Σ. We have*

$$
(\Delta_h \phi, \psi)_h = -(\nabla_h \phi, \nabla_h \psi)_h.
\tag{29}
$$

Proof. Let us first prove that $(\mathbf{1}, \nabla_h \cdot (\phi \nabla_h \psi))_h = 0$. According to the discrete divergence operator defined in Eq. (12), we have

$$
\begin{aligned}
&(\mathbf{1}, \nabla_h \cdot (\phi \nabla_h \psi))_h \\
&= \frac{1}{A(\mathbf{p})} \sum_{\mathbf{p}_i \in P} ((\sum_{j=0}^{s-1} \frac{\|\mathbf{G}_{j+1} - \mathbf{G}_j\|}{6} (2\left\langle (\phi \nabla_h \psi)(\mathbf{G}_j), \mathbf{n}(\mathbf{G}_j)\right\rangle + 2\left\langle (\phi \nabla_h \psi)(\mathbf{G}_{j+1}), \mathbf{n}(\mathbf{G}_{j+1})\right\rangle \\
&\quad + \left\langle (\phi \nabla_h \psi)(\mathbf{G}_j), \mathbf{n}(\mathbf{G}_{j+1})\right\rangle + \left\langle (\phi \nabla_h \psi)(\mathbf{G}_{j+1}), \mathbf{n}(\mathbf{G}_j)\right\rangle)))) \\
&= \sum_{\overline{\mathbf{G}_j \mathbf{G}_{j+1}} \in \tilde{P}} \frac{\|\mathbf{G}_j - \mathbf{G}_{j+1}\|}{6} ((2\left\langle \nabla_h \cdot (\phi \nabla_h \psi)(\mathbf{G}_j), \mathbf{n}(\mathbf{G}_j)\right\rangle \\
&\quad + 2\left\langle \nabla_h \cdot (\phi \nabla_h \psi)(\mathbf{G}_{j+1}), \mathbf{n}(\mathbf{G}_{j+1})\right\rangle + \left\langle \nabla_h \cdot (\phi \nabla_h \psi)(\mathbf{G}_j), \mathbf{n}(\mathbf{G}_{j+1})\right\rangle + \left\langle \nabla_h \cdot (\phi \nabla_h \psi)(\mathbf{G}_{j+1}), \mathbf{n}(\mathbf{G}_j)\right\rangle) \\
&\quad + (2\left\langle \nabla_h \cdot (\phi \nabla_h \psi)(\mathbf{G}_j), \mathbf{n}(\mathbf{G}_j)\right\rangle + 2\left\langle \nabla_h \cdot (\phi \nabla_h \psi)(\mathbf{G}_{j+1}), \mathbf{n}(\mathbf{G}_{j+1})\right\rangle \\
&\quad + \left\langle \nabla_h \cdot (\phi \nabla_h \psi)(\mathbf{G}_i), \mathbf{n}(\mathbf{G}_{j+1})\right\rangle + \left\langle \nabla_h \cdot (\phi \nabla_h \psi)(\mathbf{G}_{j+1}), \mathbf{n}(\mathbf{G}_j)\right\rangle)) \\
&= \sum_{\overline{\mathbf{G}_j \mathbf{G}_{j+1}} \in \tilde{P}} \frac{\|\mathbf{G}_j - \mathbf{G}_{j+1}\|}{6} (2\left\langle \nabla_h \cdot (\phi \nabla_h \psi)(\mathbf{G}_j), \mathbf{n}_{\mathbf{p}_{j+1}}(\mathbf{G}_j) + \mathbf{n}_{\mathbf{p}}(\mathbf{G}_j)\right\rangle \\
&\quad + 2\left\langle \nabla_h \cdot (\phi \nabla_h \psi)(\mathbf{G}_{j+1}), \mathbf{n}_{\mathbf{p}_{j+1}}(\mathbf{G}_{j+1}) + \mathbf{n}_{\mathbf{p}}(\mathbf{G}_{j+1})\right\rangle \\
&\quad + \left\langle \nabla_h \cdot (\phi \nabla_h \psi)(\mathbf{G}_j), \mathbf{n}_{\mathbf{p}_{j+1}}(\mathbf{G}_{j+1}) + \mathbf{n}_{\mathbf{p}}(\mathbf{G}_{j+1})\right\rangle \\
&\quad + \left\langle \nabla_h \cdot (\phi \nabla_h \psi)(\mathbf{G}_{j+1}), \mathbf{n}_{\mathbf{p}_{j+1}}(\mathbf{G}_j) + \mathbf{n}_{\mathbf{p}}(\mathbf{G}_j)\right\rangle) = 0.
\end{aligned}
\tag{30}
$$

Here we have used the definition of the dual mesh and Eq. (28). Then let us prove Theorem 3:

$$
\begin{aligned}
&(\phi, \Delta_h \psi)_h = (\phi, \Delta_h \psi)_h - (\mathbf{1}, \nabla_h \cdot (\phi \nabla_h \psi))_h \\
&= \sum_{\mathbf{p}_i \in P} A(\mathbf{p}_i) \phi_i \frac{1}{A(\mathbf{p}_i)} \sum_{j=0}^{s-1} \frac{\|\mathbf{G}_{j+1} - \mathbf{G}_j\|}{6} (2\left\langle \nabla_h \psi(\mathbf{G}_j), \ \mathbf{n}(\mathbf{G}_j)\right\rangle + 2\left\langle \nabla_h \psi(\mathbf{G}_{j+1}), \ \mathbf{n}(\mathbf{G}_{j+1})\right\rangle \\
&\quad + \left\langle \nabla_h \psi(\mathbf{G}_j), \ \mathbf{n}(\mathbf{G}_{j+1})\right\rangle + \left\langle \nabla_h \psi(\mathbf{G}_{j+1}), \ \mathbf{n}(\mathbf{G}_j)\right\rangle) \\
&\quad - \sum_{\mathbf{p}_i \in P} \frac{1}{A(\mathbf{p}_i)} \left(\sum_{j=0}^{s-1} \frac{\|\mathbf{G}_{j+1} - \mathbf{G}_j\|}{6} (2\left\langle \phi \nabla_h \psi(\mathbf{G}_j), \ \mathbf{n}(\mathbf{G}_j)\right\rangle + 2\left\langle \phi \nabla_h \psi(\mathbf{G}_{j+1}), \ \mathbf{n}(\mathbf{G}_{j+1})\right\rangle \right. \\
&\quad \left. + \left\langle \phi \nabla_h \psi(\mathbf{G}_j), \ \mathbf{n}(\mathbf{G}_{j+1})\right\rangle + \left\langle \phi(\mathbf{G}_j) \nabla_h \psi(\mathbf{G}_{j+1}), \ \mathbf{n}(\mathbf{G}_j)\right\rangle) \right) A(\mathbf{p}_i) \\
&= \sum_{\mathbf{p}_i \in P} \sum_{j=0}^{s-1} \left(\left\langle \nabla_h \psi(\mathbf{G}_j), \ \frac{\|\mathbf{G}_{j+1} - \mathbf{G}_j\|}{3} (\phi(\mathbf{p}_i) - \phi(\mathbf{G}_j)) \cdot \mathbf{n}(\mathbf{G}_j)\right\rangle \right.
\end{aligned}
$$

$$+ \left\langle \nabla_h \psi(\mathbf{G}_{j+1}), \ \frac{\|\mathbf{G}_{j+1} - \mathbf{G}_j\|}{3} (\phi(\mathbf{p}_i) - \phi(\mathbf{G}_{j+1})) \cdot \mathbf{n}(\mathbf{G}_{j+1}) \right\rangle$$

$$+ \left\langle \nabla_h \psi(\mathbf{G}_j), \ \frac{\|\mathbf{G}_{j+1} - \mathbf{G}_j\|}{6} (\phi(\mathbf{p}_i) - \phi(\mathbf{G}_j)) \cdot \mathbf{n}(\mathbf{G}_{j+1}) \right\rangle$$

$$+ \left\langle \nabla_h \psi(\mathbf{G}_{j+1}), \ \frac{\|\mathbf{G}_{j+1} - \mathbf{G}_j\|}{6} (\phi(\mathbf{p}_i) - \phi(\mathbf{G}_{j+1})) \cdot \mathbf{n}(\mathbf{G}_j) \right\rangle \Big)$$

$$= \sum_{\mathbf{p}_i \in P} \sum_{j=0}^{s-1} \left\langle \nabla_h \psi(\mathbf{G}_j), \ \frac{\|\mathbf{G}_{j+1} - \mathbf{G}_j\|}{6} (\phi(\mathbf{p}_i) - \phi(\mathbf{G}_j)) \cdot \big(2\mathbf{n}(\mathbf{G}_j) + \mathbf{n}(\mathbf{G}_{j+1})\big) \right\rangle$$

$$+ \sum_{\mathbf{p}_i \in P} \sum_{j=1}^{s} \left\langle \nabla_h \psi(\mathbf{G}_j), \ \frac{\|\mathbf{G}_j - \mathbf{G}_{j-1}\|}{6} (\phi(\mathbf{p}_i) - \phi(\mathbf{G}_j)) \cdot \big(2\mathbf{n}(\mathbf{G}_j) + \mathbf{n}(\mathbf{G}_{j-1})\big) \right\rangle$$

$$= \sum_{\mathbf{p}_i \in P} \sum_{j=0}^{s-1} \left\langle \nabla_h \psi(\mathbf{G}_j), \ (\phi(\mathbf{p}_i) - \phi(\mathbf{G}_j)) \cdot \left(\frac{\|\mathbf{G}_{j+1} - \mathbf{G}_j\|}{6} \big(2\mathbf{n}(\mathbf{G}_j) + \mathbf{n}(\mathbf{G}_{j+1})\big) \right. \right.$$

$$\left. \left. + \frac{\|\mathbf{G}_j - \mathbf{G}_{j-1}\|}{6} \big(2\mathbf{n}(\mathbf{G}_j) + \mathbf{n}(\mathbf{G}_{j-1})\big) \right) \right\rangle$$

$$= \sum_{\mathbf{p}_i \in P} \sum_{j=0}^{s-1} \Big\langle \nabla_h \psi(\mathbf{G}_j), (\phi(\mathbf{p}_i) - \phi(\mathbf{G}_j))$$

$$\cdot \left(\frac{\|\mathbf{G}_{j+1} - \mathbf{G}_j\|}{6} \Big(2 \frac{(\mathbf{G}_{j+1} - \mathbf{G}_j) \times (\mathbf{p}_j - \mathbf{G}_j) \times (\mathbf{p}_{j+1} - \mathbf{G}_j)}{\|(\mathbf{G}_{j+1} - \mathbf{G}_j) \times (\mathbf{p}_j - \mathbf{G}_j) \times (\mathbf{p}_{j+1} - \mathbf{G}_j)\|} \right.$$

$$+ \frac{(\mathbf{G}_{j+1} - \mathbf{G}_j) \times (\mathbf{p}_{j+2} - \mathbf{G}_{j+1}) \times (\mathbf{p}_{j+1} - \mathbf{G}_{j+1})}{\|(\mathbf{G}_{j+1} - \mathbf{G}_i) \times (\mathbf{p}_{j+2} - \mathbf{G}_{j+1}) \times (\mathbf{p}_{j+1} - \mathbf{G}_{j+1})\|} \Big)$$

$$+ \frac{\|\mathbf{G}_j - \mathbf{G}_{j-1}\|}{6} \Big(2 \frac{(\mathbf{G}_{j+1} - \mathbf{G}_j) \times (\mathbf{p}_j - \mathbf{G}_j) \times (\mathbf{p}_{j+1} - \mathbf{G}_j)}{\|(\mathbf{G}_{j+1} - \mathbf{G}_j) \times (\mathbf{p}_j - \mathbf{G}_j) \times (\mathbf{p}_{j+1} - \mathbf{G}_j)\|}$$

$$\left. \left. + \frac{(\mathbf{G}_j - \mathbf{G}_{j-1}) \times (\mathbf{p}_{j-1} - \mathbf{G}_{j-1}) \times (\mathbf{p}_j - \mathbf{G}_{j-1})}{\|(\mathbf{G}_j - \mathbf{G}_{j-1}) \times (\mathbf{p}_{j-1} - \mathbf{G}_{j-1}) \times (\mathbf{p}_j - \mathbf{G}_{j-1})\|} \Big) \right) \right\rangle$$

$$= \sum_{\mathbf{p}_i \in P} \sum_{j=0}^{s-1} \Big\langle \nabla_h \psi(\mathbf{G}_j), \frac{A(\mathbf{p}_i)}{|B_i|} \Big(\Big(\langle \mathbf{p}_{j+1} - \mathbf{G}_j, \mathbf{p}_{j+1} - \mathbf{G}_j \rangle \|\mathbf{p} - \mathbf{G}_j\|^2$$

$$- \langle \mathbf{p}_{j+1} - \mathbf{G}_j, \mathbf{p}_{j+1} - \mathbf{G}_j \rangle \|\mathbf{p}_j - \mathbf{G}_j\|^2 \Big)(\phi(\mathbf{p}_i) - \phi(\mathbf{G}_j)) + \Big(\langle \mathbf{p}_j - \mathbf{G}_j, \mathbf{p}_{j+1} - \mathbf{G}_j \rangle \|\mathbf{p}_j - \mathbf{G}_j\|^2$$

$$- \langle \mathbf{p}_j - \mathbf{G}_j, \mathbf{p}_j - \mathbf{G}_j \rangle \|\mathbf{p}_{j+1} - \mathbf{G}_j\|^2 \Big)(\phi(\mathbf{p}_j) - \phi(\mathbf{G}_j))$$

$$+ \Big(\langle \mathbf{p}_j - \mathbf{G}_j, \mathbf{p}_j - \mathbf{G}_j \rangle \langle \mathbf{p}_{j+1} - \mathbf{G}_j, \mathbf{p}_{j+1} - \mathbf{G}_j \rangle$$

$$- \langle \mathbf{p}_j - \mathbf{G}_j, \mathbf{p}_{j+1} - \mathbf{G}_j \rangle \langle \mathbf{p}_{j+1} - \mathbf{G}_j, \mathbf{p}_j - \mathbf{G}_j \rangle \Big)(\phi(\mathbf{p}_{j+1}) - \phi(\mathbf{G}_j)) \Big)$$

$$+ \frac{A(\mathbf{p}_i)}{|B_i|} \Big(\Big(\langle \mathbf{p}_{j+1} - \mathbf{G}_j, \mathbf{p}_{j+1} - \mathbf{G}_j \rangle \|\mathbf{p} - \mathbf{G}_i\|^2$$

$$- \langle \mathbf{p}_{j+1} - \mathbf{G}_j, \mathbf{p}_i - \mathbf{G}_j \rangle \|\mathbf{p}_{j+1} - \mathbf{G}_j\|^2 \Big)(\phi(\mathbf{p}_i) - \phi(\mathbf{G}_j))$$

$$+ \Big(\langle \mathbf{p}_j - \mathbf{G}_j, \mathbf{p} - \mathbf{G}_j \rangle \|\mathbf{p}_{j+1} - \mathbf{G}_j\|^2 - \langle \mathbf{p}_j - \mathbf{G}_j, \mathbf{p}_{j+1} - \mathbf{G}_j \rangle \|\phi(\mathbf{p}_j) - \phi(\mathbf{G}_j)\|^2 \Big)(\phi(\mathbf{p}_j) - \phi(\mathbf{G}_j))$$

$$+ \Big(\langle \mathbf{p}_j - \mathbf{G}_j, \mathbf{p}_j - \mathbf{G}_j \rangle \langle \mathbf{p}_{j+1} - \mathbf{G}_j, \mathbf{p}_{j+1} - \mathbf{G}_j \rangle$$

$$- \langle \mathbf{p}_j - \mathbf{G}_j, \mathbf{p}_{j+1} - \mathbf{G}_j \rangle \langle \mathbf{p}_{j+1} - \mathbf{G}_j, \mathbf{p}_j - \mathbf{G}_j \rangle \Big) (\phi(\mathbf{p}_{j+1}) - \phi(\mathbf{G}_j)) \Big) \Big\rangle$$

$$= - \sum_{\mathbf{p}_i \in P} \sum_{j=0}^{s-1} \Big\langle \nabla_h \psi(\mathbf{G}_j), \ A(\mathbf{p}_i) \Big(\alpha_j (\mathbf{p}_j - \mathbf{G}_j) + \beta_j (\mathbf{p}_{j+1} - \mathbf{G}_j) \Big) \Big\rangle$$

$$= - \sum_{\mathbf{p}_i \in P} \left(A(\mathbf{p}_i) \sum_{j=0}^{s-1} \nabla_h \phi(\mathbf{G}_j) \cdot \nabla_h \psi(\mathbf{G}_j) \right) = - (\nabla_h \phi, \nabla_h \psi)_h \qquad (31)$$

which corresponds to Eq. (29). Here we have used the definition of the outer normal vector $\mathbf{n}_p(\mathbf{G}_j)$ in Eq. (5) and the discrete gradient of the vector field $\nabla_h \mathbf{X}(\mathbf{G}_j)$ in Eq. (7). $\square$

Several summarizations of our proposed method are remarked here: (i) The discrete CHNS scheme (17) is a three-level scheme and we need to set initial step ϕ^{-1} at every time step for the second-order accuracy. In this work, $\phi^{-1} := \phi^0$ is used. Although the setting of this initial condition reduces the accuracy of the first time step, it does not affect the overall accuracy to be second-order. Thus, second-order accuracy with respect to time and space can be obtained during the whole simulation. (ii) Although the discrete method is of three-time-levels, the results of first time level ϕ^{n-1} do not appear in the energy dissipation result. That is because the term $\frac{\Delta t \sigma \rho}{\epsilon}(\tilde{\phi}^{n+\frac{1}{2}}\nabla_h \mu^{n+\frac{1}{2}}, \hat{\mathbf{v}}^{n+\frac{1}{2}})$ in Eq. (18) has been canceled out during the computation. Similarly, the results of first time level ϕ^{n-1} do not appear in the mass conservation theorem because the terms of $(\nabla_h \mu^{n+\frac{1}{2}}/Pe + \tilde{\phi}^{n+\frac{1}{2}}\hat{\mathbf{v}}^{n+\frac{1}{2}})(\mathbf{G}_j)$ and $(\nabla_h \mu^{n+\frac{1}{2}}/Pe + \tilde{\phi}^{n+\frac{1}{2}}\hat{\mathbf{v}}^{n+\frac{1}{2}})(\mathbf{G}_{j+1})$ have been canceled out during the computation. (iii) The discrete energy dissipation and mass conservation can be obtained for various complex curved surfaces. (iv) Our proposed method can be directly applied to multiphase flow model.

4. Solutions for CHNS systems

In this section, we present the numerical solutions of our proposed incompressible CHNS system. Since the phase motion is strongly coupled with the velocity field evolution, it is significant to solve the NS and CH equations in a temporally matched manner.

4.1. Cahn–Hilliard solver

Given the initial $\mathbf{v}_i^{n-1}$, $\mathbf{v}_i^n$, ϕ_i^{n-1} and ϕ_i^n, we want to find ϕ_i^{n+1} and $\mu_i^{n+\frac{1}{2}}$ by the following equations

$$\begin{cases} \dfrac{\phi_i^{n+1} - \phi_i^n}{\Delta t} + \nabla_h \cdot \left(\tilde{\phi}_i^{n+\frac{1}{2}} \hat{\mathbf{v}}_i^{n+\frac{1}{2}} \right) = \epsilon \Delta_h \mu_i^{n+\frac{1}{2}}, \\[2mm] \mu_i^{n+\frac{1}{2}} = g(\phi_i^{n+1}) - \epsilon^2 \dfrac{\Delta_h \phi_i^{n+1} + \Delta_h \phi_i^n}{2}, \end{cases} \qquad (32)$$

where $g(\phi_i^{n+1}) := (f(\phi_i^{n+1}) - f(\phi_i^n))/(\phi_i^{n+1} - \phi_i^n)$ is defined as the chemical potential term. Since $g(\phi_i^{n+1})$ in Eq. (32) is nonlinear with respect to ϕ_i^{n+1}, we linearize $g(\phi_i^{n+1,m})$ at $\phi_i^{n+1,m}$, i.e.,

$$\begin{aligned} g(\phi_i^{n+1,m}) &= 0.25 \Big((\phi_i^{n+1,m})^3 + (\phi_i^n - 2)(\phi_i^{n+1,m})^2 + (\phi_i^n - 1)^2 \phi_i^{n+1,m} + \phi_i^n (\phi_i^n - 1)^2 \Big) \\ &= 0.25 \Big((\phi_i^{n+1,m-1})^3 + (\phi_i^n - 2)(\phi_i^{n+1,m-1})^2 + (\phi_i^n - 1)^2 \phi_i^{n+1,m-1} + \phi_i^n (\phi_i^n - 1)^2 \\ &\quad + (3(\phi_i^{n+1,m-1})^2 + 2(\phi_i^n - 2)\phi_i^{n+1,m-1} + (\phi_i^n - 1)^2)(\phi_i^{n+1,m} - \phi_i^{n+1,m-1}) \Big). \end{aligned} \qquad (33)$$

A Jacobi-type iteration is applied to solve Eq. (32):

$$\begin{cases} \dfrac{\phi_i^{n+1,m} - \phi_i^n}{\Delta t} + \nabla_h \cdot \left(\tilde{\phi}_i^{n+\frac{1}{2}} \hat{\mathbf{v}}_i^{n+\frac{1}{2}} \right) = \epsilon \Delta_h \mu_i^{n+\frac{1}{2},m}, \\[2mm] \mu_i^{n+\frac{1}{2},m} = g(\phi_i^{n+1,m}) - \epsilon^2 \dfrac{\Delta_h \phi_i^{n+1,m} + \Delta_h \phi_i^n}{2}, \end{cases} \qquad (34)$$

Here we denote m as the index of Jacobi iteration and the initial condition $\phi_i^{n+1,0}$ is defined as $\phi_i^{n+1,0} = 2\phi_i^n - \phi_i^{n-1}$. Herein, Eq. (34) becomes a linear system with respect to $\phi_i^{n+1,m}$ and $\mu_i^{n+\frac{1}{2},m}$ and can be solved with a biconjugate gradient stabilized method. We execute the procedure (Eq. (34)) until the error is smaller than a given tolerance *tol* as:

$$\|\phi_i^{n+1,m} - \phi_i^{n+1,m-1}\|_h \leq tol.$$

Then we will set $\phi_i^{n+1} = \phi_i^{n+1,m}$. The residual error converges rather quickly to a tolerance $tol = 1e-6$ in few iterations.

4.2. Navier–Stokes solver

For the given $\mathbf{v}_i^n$ and p_i^n, we compute $\mathbf{v}_i^{n+1}$ and p_i^{n+1} with the known $\tilde{\phi}_i^{n+\frac{1}{2}}$ and $\mu_i^{n+\frac{1}{2}}$ by the following steps:

Step 1. $\left(\mathcal{I} - \dfrac{\Delta t \eta}{2\rho}\Delta_h\right)\hat{\mathbf{v}}_i^{n+1} = -\Delta t\left(\tilde{\mathbf{v}}_i^{n+\frac{1}{2}} \cdot \nabla_h \tilde{\hat{\mathbf{v}}}_i^{n+\frac{1}{2}} + \nabla_h \cdot (\tilde{\mathbf{v}}_i^{n+\frac{1}{2}} \otimes \tilde{\hat{\mathbf{v}}}_i^{n+\frac{1}{2}})\right)$

$$+ \frac{\Delta t}{\rho}\left(-\nabla_h p_i^n + \frac{\eta}{2}\Delta_h \mathbf{v}_i^n - \frac{\sigma \tilde{\phi}_i^{n+\frac{1}{2}}}{2\epsilon}\nabla_h \mu_i^{n+\frac{1}{2}}\right) + \mathbf{v}_i^n,$$

Step 2. $\Delta_h p_i^{n+1} = \Delta_h p_i^n + \dfrac{2\rho}{\Delta t}\nabla_h \cdot \hat{\mathbf{v}}_i^{n+1},$

Stpe 3. $\mathbf{v}_i^{n+1} = \dfrac{\Delta t}{2\rho}\nabla_h\left(p_i^n - p_i^{n+1}\right) + \hat{\mathbf{v}}_i^{n+1}.$

where $\mathcal{I}$ denotes the identity matrix. In **Step 1**, we apply a biconjugate gradient stabilized method to update $\hat{\mathbf{v}}_i^{n+1}$. We use the Adams–Bashforth extrapolation to deal with the convection term explicitly. **Step 2** is obtained by taking the discrete divergence operation to Eq. (17d) and using Eq. (17e). For the update of pressure, we demonstrate a Jacobi-type iteration to compute the linear equation, which has been widely used in previous studies and proved to be simple and efficient [44,45]. Since the matrix of the discrete Laplace–Beltrami operator is not strictly diagonally dominant, which may lead to results without convergence. Thus, we apply a Picard iteration as

$$\Delta_h p_i^{n+1,m} + Dp_i^{n+1,m} = \Delta_h p_i^n + Dp_i^{n+1,m-1} + \frac{2\rho}{\Delta t}\nabla_h \cdot \hat{\mathbf{v}}_i^{n+1}, \tag{35}$$

where D is a modified matrix, such that $(\Delta_h + D)$ is a diagonally dominant matrix. Here we use $D = 0.01\mathcal{I}$. **Step 3** is applied until the convergence condition is satisfied with a given tolerance as

$$\|p_i^{n+1,m} - p_i^{n+1,m-1}\|_h \leq tol, \tag{36}$$

where $p_i^{n+1,m}$ and $p_i^{n+1,m-1}$ are the solutions of the mth and $(m-1)$th iterations. Here we choose $p_i^{n+1,0} = p^n$ and let $p_i^{n+1} = p^{n+1,m}$. Finally, $\mathbf{v}_i^{n+1}$ can be obtained with the calculated p_i^{n+1} and $\hat{\mathbf{v}}_i^{n+1}$ in **Step 3**.

5. Numerical experiments

5.1. Non-increasing discrete energy and mass conservation

To demonstrate the unconditional energy dissipation and mass conservation, we consider the phase variable ϕ on a unit sphere surface. Let us denote $\mathbf{v} := (u, v, w)$. The initial condition is chosen as follows:

$$\begin{cases} \phi(x, y, z, 0) = \text{rand}(x, y, z), \quad p(x, y, z, 0) = 1, \\ u(x, y, z, 0) = 1, \quad v(x, y, z, 0) = 1, \quad w(x, y, z, 0) = 1, \end{cases}$$

where $\text{rand}(x, y, z)$ is a random number between 0 and 1. The mass of phase variables can be defined as $M := \sum_{i=1}^{N_P} \phi_i A(\mathbf{p}_i)$, where $A(\mathbf{p}_i)$ is defined as the area of polygon around the ith vertex. Here, we consider the parameters as: $h = 0.08$, $\Delta t = 2.5h$, $\rho = 1$, $\eta = 1$, $\epsilon = 0.04$, $Pe = 1/\epsilon$ and $\sigma = \epsilon$. The results shown in Fig. 2 suggest that the phases are gathered together and the interface between phases has evolved due to the hydrodynamic phase field model. It should be noted that the difference between the discrete original energy and discrete modified energy
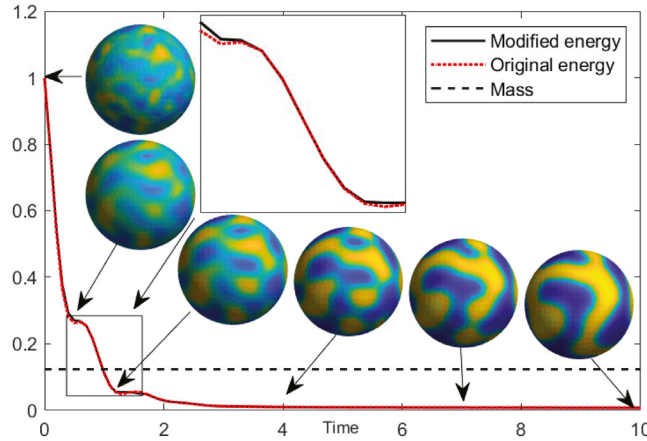
Fig. 2. Temporal evolution of the non-increasing discrete modified energy, original energy and mass conservation of the proposed method. The inset figures are the morphology of the phase field at the indicated times. Note that the modified energy and original energy have been normalized by the initial energy. The discrete original energy and discrete modified energy dissipate, which verifies that the proposed scheme is stable.

dissipates, i.e., $\Delta t^2 \|\nabla_h p^n\|^2/(8\rho)$, which is second order respect to Δt, is much small. Furthermore, we can observe that the mass is conserved and the discrete original energy and discrete modified energy dissipate, which verifies that the proposed scheme is stable.

5.2. Stability of the proposed scheme

Since the NS equation contains the strong nonlinear term, i.e. the convention term, and the CH equation contains the fourth-order spatial derivatives, i.e. the chemical potential term, the explicit time scheme leads to severe time-step restrictions for stability. To demonstrate the stability of our proposed scheme, we perform the numerical experiment with $\Delta t = 10,\ 1,\ 0.1$ and 0.01, respectively. The initial conditions are

$$\begin{cases} \phi(x, y, z, 0) = 0.5 + 0.5 \sin(2\pi x) \sin(2\pi y) \sin(2\pi z), \\ u(x, y, z, 0) = 0,\ \ v(x, y, z, 0) = 0,\ \ w(x, y, z, 0) = 0,\ \ p(x, y, z, 0) = 0. \end{cases}$$

The parameters are set the same as in Section 5.1. As shown in Fig. 3, we compare the temporal evolution of the total energy for four different time steps $\Delta t = 10, 1, 0.1$ and 0.01 until $t = 1000$. The inset figures are the morphology of the phase field at the indicated times with $\Delta t = 10$. As can be seen, no blow-up of the numerical solutions is present and the discrete modified energies with different time steps are non-increasing, which implies that large time steps can be used in our scheme. We find that the results with $\Delta t = 0.1$ are in good agreement with the results for the smaller time step $\Delta t = 0.01$. However, these differ from the results for the larger time step $\Delta t = 1$. We can observe that the results with a large time step are less accurate than those obtained by using a small time step because using a larger time step would cause large error of the numerical solutions. Therefore, a small time step will be used for highly accurate numerical solutions. Therefore, to maintain our proposed scheme's accuracy and reduce computational costs, an appropriate value for Δt is $\Delta t = 0.1$.

5.3. Convergence test

In this section, we perform two numerical experiments to demonstrate the convergence of the proposed second-order spatial and temporal numerical scheme. In order to avoid the influence of the geometry and structure of the mesh grid, we use a unit sphere to generate a set of high-quality mesh grids, which has almost the same edge in all triangles. In order to obtain the convergence rate for temporal discretization with the same spatial step size $h = 0.025$, we choose a set of different time steps such as $\Delta t = 8e\text{–}4, 4e\text{–}4, 2e\text{–}4$ and $1e\text{–}4$. The results are run up to time $t = 0.1$ with the same initial condition $\phi(x, y, z, 0) = 0.5 + 0.5 \sin(2\pi x) \sin(2\pi y) \sin(2\pi z)$. The parameters
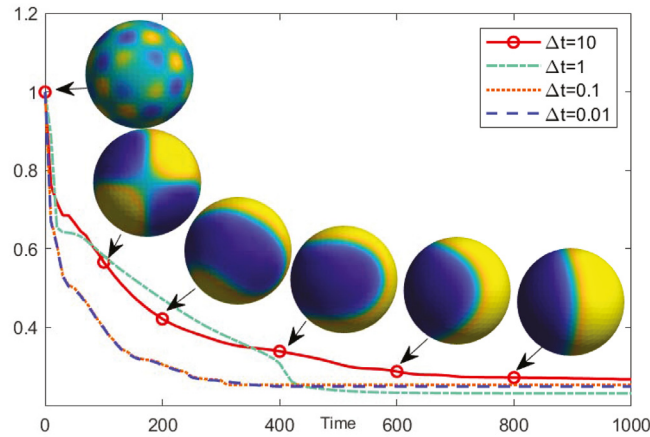
Fig. 3. Temporal evolution of the free energy functional of the proposed model for four time step sizes of $\Delta t = 10$, 1, 0.1 and 0.01. Note that the modified energy and original energy have been normalized by the initial energy. The inset figures are the morphology of the phase field at the indicated time with $\Delta t = 10$.

Table 1

Error and convergence rate of the proposed schemes with various time steps. The space step size is fixed as $h = 0.05$. The numerical reference solution is obtained with $\Delta t = 2e{-}5$ at time $t = 0.1$.

Δt	8e−4		4e−4		2e−4		1e−4
l_2 error	3.724e−7		9.081e−8		2.223e−8		5.519e−9
Rate		2.04		2.03		2.01	

Table 2

Error and convergence rate of the proposed schemes with various mesh grids. The temporal step size is fixed as $\Delta t = 5e{-}4$. The numerical reference solution is obtained with $h = 0.005$ at time $t = 0.1$.

h	0.2		0.1		0.05		0.025
l_2 error	3.690e−2		1.014e−2		1.715e−3		3.411e−4
Rate		1.86		2.56		2.33	

are set as $\epsilon = 0.1$, $\sigma = \epsilon/10$, $\rho = 1$, $\eta = 1$. Due to the lack of closed-form analytical solution, we assume that the numerical solution is generated by a very fine time step $\Delta t = 2e{-}5$ as a reference solution ϕ^{ref}. Here, the error is defined as the difference between that grid and the reference solution cell, i.e., $e_{i,\Delta t} := \phi_{i,\Delta t} - \phi_i^{\mathrm{ref}}$. The rate of convergence is defined as the ratio of successive errors: $log_2(\|e_{i,\Delta t}\|_2/\|e_{i,\Delta t/2}\|_2)$. We present the errors and the rates of convergence in Table 1. As expected from the discrete scheme Eqs. (17), our method is indeed second-order accuracy with respect to time. To demonstrate the second order spatial accuracy of our method, we first define e_{hi} as the discrete l_2-norm of the difference between the targeting grid and the average of the reference solution cells neighboring it. Here, the error is denoted as $e_{i,h} := \phi_{i,d} - \left(\zeta_i\phi_p^{\mathrm{ref}} + \eta_i\phi_q^{\mathrm{ref}} + \theta_i\phi_r^{\mathrm{ref}}\right)$, where p, q and r are the fine reference grid indexes in the triangle and the weighting coefficients ζ, η, θ are determined by $\mathbf{v}_{i,d} := \zeta_i\mathbf{v}_p^{\mathrm{ref}} + \eta_i\mathbf{v}_q^{\mathrm{ref}} + \theta_i\mathbf{v}_r^{\mathrm{ref}}$. We use $\log_2\left(\left\|e_{i,h}\right\|_2 / \left\|e_{i,h/2}\right\|_2\right)$ to denote the rate of convergence. The results are shown in Table 2. The fixed time step $\Delta t = 5e{-}4$ is used here. The results are compared at the same time $t = 0.1$. For the justification of this computation, we perform a very fine space grid $h = 0.005$. As shown in Table 2, we can see that our method is indeed second-order accuracy with respect to space.

5.4. Spinodal decomposition on an adaptive surface mesh

In this section, we use two representative meshes to show the robustness and practicability of our algorithm. The two grids are screw surface with heterogeneous mesh and bumpy sphere surface with poor-quality mesh, respectively.
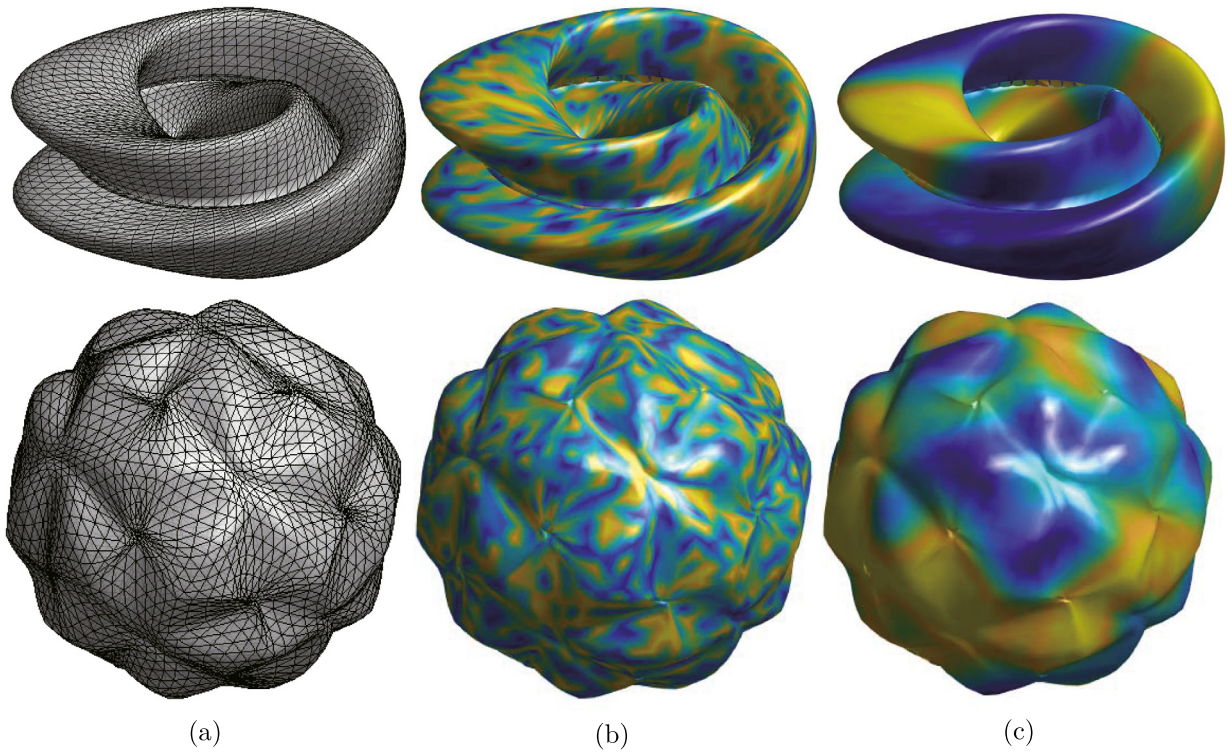
(a)   (b)   (c)

Fig. 4. Spinodal decomposition over a screw surface with nonuniform mesh and a bumpy sphere with poor-quality mesh. From left to right, the sub-figures show the surface mesh structure, the initial plots of ϕ and the final plots of ϕ, respectively.

Table 3
Value of the average divergence for the two representative meshes at various moments.

Time	0.001	0.002	0.004	0.008	0.012	0.016	0.02
Screw surface	3.61e−4	1.10e−4	2.02e−4	2.71e−4	−4.80e−5	−3.43e−4	−3.91e−4
Bumpy sphere	4.32e−4	3.11e−4	2.40e−4	1.73e−5	−3.22e−4	−2.11e−4	7.93e−5

Generally, the results are affected by the quality of the grids. The existing algorithms are simulated by using uniform grids, which is not universal. The discrete divergence operator and gradient operator over triangular surfaces may not be convergent while the adaptive mesh is used. Meanwhile, the divergence-free condition and mass conservation condition cannot be guaranteed [46]. Additionally, the discrete Laplace–Beltrami operator, which is defined by the other two operators, may lead to unstable results during the computation of CHNS system. In order to show that our proposed method is not affected by the quality of mesh, we solve the hydrodynamic phase field model over the two meshes as shown in Fig. 4. Here, the initial condition is $\phi(x, y, z, 0) = \text{rand}(x, y, z)$, where rand is a random number between 0 and 1. The parameters are chosen as follows: $h = 0.001$, $\Delta t = 0.1h$, $\epsilon = 0.1$, $Pe = 1/\epsilon$, $\sigma = 0.05$, $\rho = 1$ and $\eta = 1$. As shown in the top line of Fig. 4(a), the mesh size gets smaller as it gets closer to the center of the screw surface. The bottom figure shows the poor-quality mesh on the bumpy sphere. Fig. 4(b) shows the initial phase morphology and Fig. 4(c) is the phase morphology at $t = 0.02$. These results confirm that our method can perform well on the mesh with poor-quality and heterogeneous grid. Furthermore, we calculate the average divergence of the total points over the two surfaces and list the values of the average divergence at various specific moments as shown in Table 3. It is obvious that the average divergence of the velocity field is approximately zero, which corresponds to the physics context.
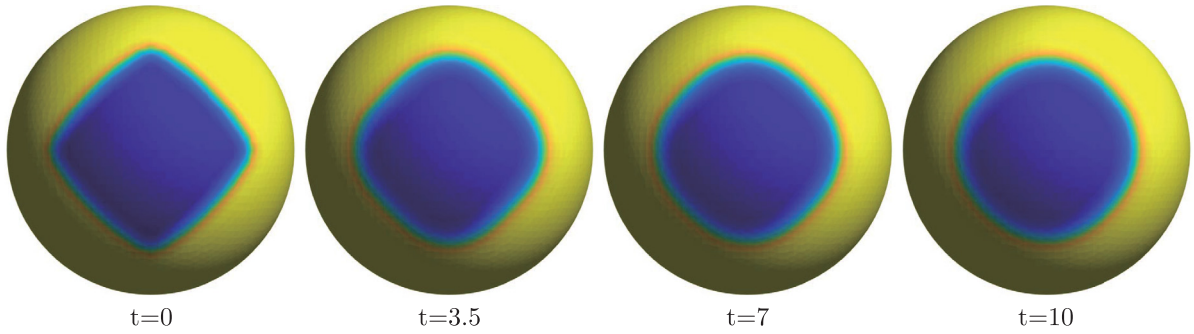
Fig. 5. Snapshots of the relaxation of a square shape by the CHNS system. From left to right, $t = 0$, 3.5, 7, 10, respectively.
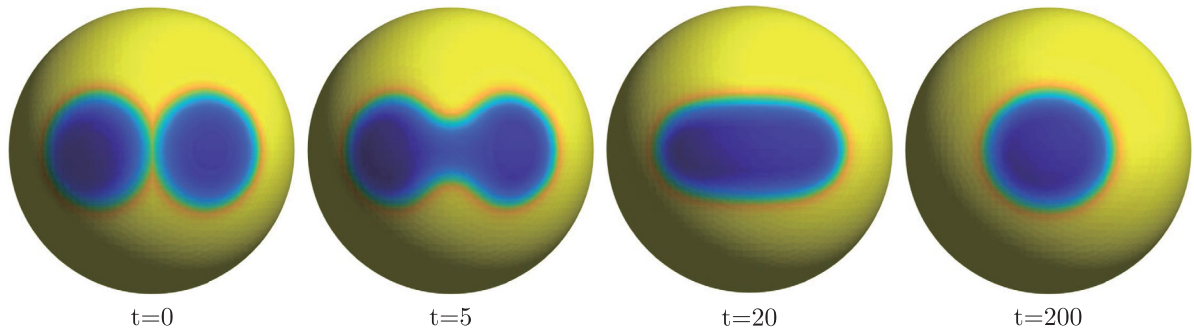

Fig. 6. The evolution of merging and the relaxation of two kissing circle by the proposed CHNS system. From left to right, $t = 0$, 5, 20 and 200, respectively.

5.5. Shape relaxation on surfaces

In this section, we use the proposed CHNS scheme to simulate the shape relaxation with the binary phases flow as shown in Figs. 5 and 6. For the first numerical experiment, we use a square as the initial shape over a unit sphere surface. The initial conditions are defined as

$$
\begin{cases}
\phi(x, y, z, 0) = 0.5 + 0.5 \tanh\left(\dfrac{|x - 1| + |y| + |z| - 1}{\sqrt{5}\epsilon}\right), \\
u(x, y, z, 0) = v(x, y, z, 0) = w(x, y, z, 0) = 0, \quad p(x, y, z, 0) = 0.
\end{cases}
$$

The parameters used here are chosen as follows: $h = 0.04$, $\Delta t = 0.1$, $\epsilon = 0.03$, $Pe = 1/\epsilon$, $\sigma = 0.001$, ρ and η are constant. Since the velocity is zero at $t = 0$, there is only the surface energy in the whole system. As we expected, the isolated irregular interface relaxes to a circle due to the isotropy of the mobility and the effect of surface tension.

For the second numerical test, we apply the merging process of two circular bubbles on a unit sphere. Under the influence of surface tension, the two circular bubbles which are tangent to each other, are merged under the influence of surface tension. They eventually relax to a large circle at which the total energy is small. The initial conditions are

$$
\begin{cases}
\phi(x, y, z, t) = 0.5 + 0.5 \tanh\left(\dfrac{\sqrt{(x - 0.55)^2 + (|y| - 0.25)^2 + z^2} - 0.5}{\sqrt{2}\epsilon}\right), \\
u(x, y, z, 0) = v(x, y, z, 0) = w(x, y, z, 0) = 0, \quad p(x, y, z, 0) = 0,
\end{cases}
$$

The parameters used here are $h = 0.04$, $\Delta t = 0.1h$, $\epsilon = 0.03$, $Pe = 1/\epsilon$ and $\sigma = 0.001$. In Fig. 6, we show the morphology of the phase field at $t = 0$, 5, 20 and 200, respectively. It is worth pointing out that the mass is conserved during the evolution of shape relaxation.
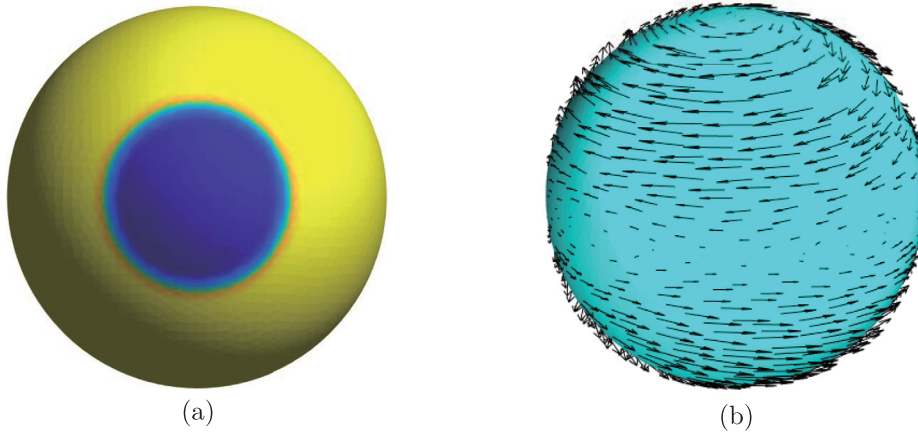
Fig. 7. Schematic illustration of the initial condition. (a) is the initial phase field and (b) is the initial velocity field.
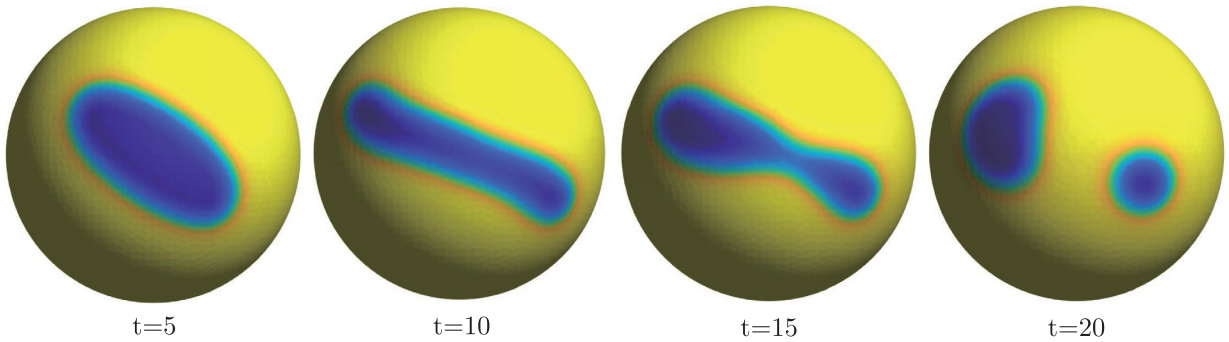

Fig. 8. From left to right are the morphology of the phase field under shear flow at $t = 5, 10, 15$ and 20, respectively.

5.6. Deformation of a drop under shear flow

Next, we simulate the deformation of a drop under the influence of shear flow. The initial ϕ and **v** are chosen as

$$
\begin{cases}
\phi(x, y, z, t) = 0.5 + 0.5 \tanh \left(\dfrac{\sqrt{(x-1)^2 + y^2 + z^2} - 0.5}{\sqrt{2}\epsilon} \right), \\
u(x, y, z, 0) = 3yz, \;\; v(x, y, z, 0) = -3xz, \;\; w(x, y, z, 0) = 0, \;\; p(x, y, z, 0) = 0,
\end{cases}
\tag{37}
$$

which has been shown in Fig. 7. The droplet of radius 0.5 is positioned at $(1, 0, 0)$ on the sphere surface. Fig. 7(b) is the initial velocity field, the top moves to the left while the bottom moves to the right over the unit sphere surface. The parameters are chosen as: $\sigma = 0.0001$ and $\epsilon = 0.03$. Here the density and viscosity are both constant. We implement this simulation with the average mesh size of $h = 0.04$ and the time step of $\Delta t = 0.1h$. We show the drop shape under shear flow obtained by our proposed method in Fig. 8. From Fig. 8(a) to (d), the indicated times are $t = 5, 10, 15$ and 20, respectively. Due to the small surface tension and high velocity at the tip of drop, fracture appears in Fig. 8(d), which corresponds with the physical context.

5.7. Simulation of Kelvin–Helmholtz instability on a sphere surface

The interface between the two fluid flows, which has a sufficiently large velocity difference, will be unstable. This interface instability is known as Kelvin–Helmholtz (KH) instability and can be observed in various natural
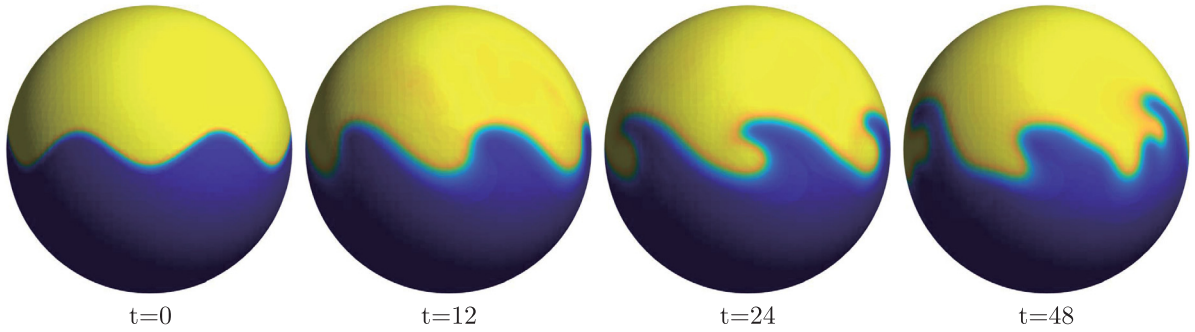
Fig. 9. The simulation of Kelvin–Helmholtz instability on a unit sphere surface. From left to right, $t = 0$, 12, 24 and 60, respectively.

situations [47]. In this section, we perform a simulation of KH instability by our proposed CHNS system over the unit sphere surface. The initial conditions are considered as

$$
\begin{cases}
\phi(x, y, z, 0) = 0.5 + 0.5 \tanh \left(\dfrac{-\cos^{-1}\left(z/\sqrt{x^2 + y^2 + z^2}\right) + 0.5\pi + 0.06\cos\left(6\tan^{-1}(y/x)\right)}{\sqrt{2}\epsilon} \right), \\
u(x, y, z, 0) = 10(\phi - 0.5)y, \quad v(x, y, z, 0) = -10(\phi - 0.5)x, \quad w(x, y, z, 0) = 0, \quad p(x, y, z, 0) = 0.
\end{cases}
$$

For this simulation, we choose the parameters as: $h = 0.025$, $\Delta t = 0.01$, $\epsilon = 0.01$ and $Pe = 10/\epsilon$. As shown in Fig. 9, we perform a long time simulation of the KH instability, which eventually develops to a disordered structure. This numerical experiment indicates that our method can be used efficiently for the computation of KH instability on complex surfaces.

5.8. Simulation of buoyancy-driven flow on a helical collar surface

In this section, we perform a simulation of rising process under the buoyancy-driven flow over a helical collar surface. The two phases are assumed to have different densities. Let us add a buoyancy term to the NS equation as follows

$$
\rho(\phi)\left(\frac{\partial \mathbf{v}(\mathbf{x}, t)}{\partial t} + \frac{\mathbf{v}(\mathbf{x}, t) \cdot \nabla_S \mathbf{v}(\mathbf{x}, t) + \nabla_S \cdot (\mathbf{v}(\mathbf{x}, t) \otimes \mathbf{v}(\mathbf{x}, t))}{2} \right)
$$
$$
= -\nabla_S p(\mathbf{x}, t) + \frac{1}{Re} \nabla_S \cdot (\eta \nabla_S \mathbf{v}(\mathbf{x}, t)) - \frac{\epsilon^{-1}}{We} \phi(\mathbf{x}, t) \nabla_S \mu(\mathbf{x}, t) + \frac{\rho(\phi) - \rho_1}{Fr^2} \mathbf{g},
$$

where $\rho = \rho_1 \phi + \rho_2(1 - \phi)$, ρ_1 and ρ_2 are the densities of two phases and $\rho_1 \leq \rho_2$. We use $\mathbf{g} := (0, \; 0, \; -1)$ to denote the gravity field and Fr is the Froude number. Since the two fluids have different densities, we modified the system Eqs. (17) as:

$$
\frac{\phi_i^{n+1} - \phi_i^n}{\Delta t} = \frac{1}{Pe} \Delta_h \mu_i^{n+\frac{1}{2}} - \nabla_h \cdot (\tilde{\phi}_i^{n+\frac{1}{2}} \hat{\mathbf{v}}_i^{n+\frac{1}{2}}), \tag{38a}
$$

$$
\mu_i^{n+\frac{1}{2}} = \frac{f(\phi_i^{n+1}) - f(\phi_i^n)}{\phi_i^{n+1} - \phi_i^n} - \epsilon^2 \Delta_h \frac{\phi_i^{n+1} + \phi_i^n}{2}, \tag{38b}
$$

$$
\rho(\phi_i^{n+\frac{1}{2}}) \frac{\hat{\mathbf{v}}_i^{n+1} - \mathbf{v}_i^n}{\Delta t} + \frac{\rho(\phi_i^{n+\frac{1}{2}})}{2} \left(\tilde{\mathbf{v}}_i^{n+\frac{1}{2}} \cdot \nabla_h \hat{\mathbf{v}}_i^{n+\frac{1}{2}} + \nabla_h \cdot \left(\tilde{\mathbf{v}}_i^{n+\frac{1}{2}} \otimes \hat{\mathbf{v}}_i^{n+\frac{1}{2}} \right) \right)
$$
$$
= -\nabla_h p_i^n + \nabla_h \cdot \left(\eta \nabla_h \hat{\mathbf{v}}_i^{n+\frac{1}{2}} \right) - \frac{\sigma \rho(\phi_i^{n+\frac{1}{2}})}{\epsilon} \tilde{\phi}_i^{n+\frac{1}{2}} \nabla_h \mu_i^{n+\frac{1}{2}} + \frac{\rho(\phi_i^{n+\frac{1}{2}}) - \rho_1}{Fr^2} \mathbf{g}, \tag{38c}
$$

$$
\rho(\phi_i^{n+\frac{1}{2}}) \frac{\mathbf{v}_i^{n+1} - \hat{\mathbf{v}}_i^{n+1}}{\Delta t} + \frac{1}{2} \nabla_h \left(p_i^{n+1} - p_i^n \right) = 0, \tag{38d}
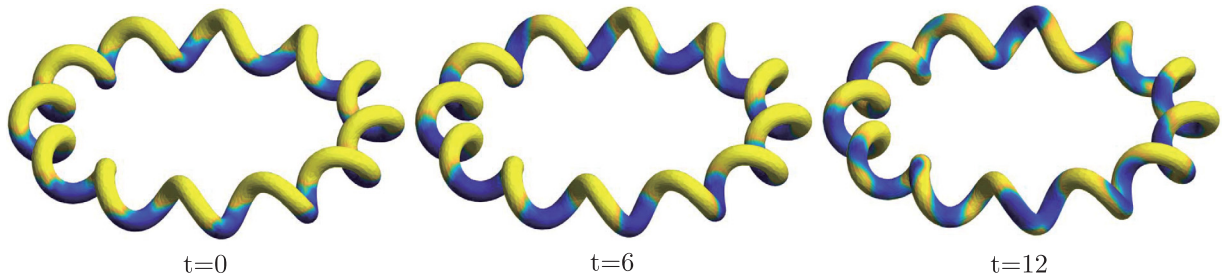$$

Fig. 10. Simulation of buoyancy-driven flow over a helical collar surface. From the left to right, $t = 0$, 6 and 12, respectively. (For interpretation of the references to color in this figure legend, the reader is referred to the web version of this article.)

$$\nabla_h \cdot \mathbf{v}_i^{n+1} = 0, \tag{38e}$$

$$\rho(\phi_i^{n+\frac{1}{2}}) = \rho_1 \phi_i^{n+\frac{1}{2}} + \rho_2 \left(1 - \phi_i^{n+\frac{1}{2}}\right). \tag{38f}$$

We have to point that the resulting method is still second-order accurate with respect to time and space, since we use the second-order Crank–Nicolson-type scheme. However, since $\rho(\phi)$ is the function of ϕ, we cannot prove the energy stability of Eq. (38c) in theory. The initial conditions are defined as

$$
\begin{cases}
\phi(x, y, z, 0) = 0.5 + 0.5 \tanh\left(\dfrac{z + 0.06\mathrm{rand}(x, y, z)}{\sqrt{2}\epsilon}\right), \\
u(x, y, z, 0) = v(x, y, z, 0) = w(x, y, z, 0) = 0, \quad p(x, y, z, 0) = 0,
\end{cases}
$$

where $\mathrm{rand}(x, y, z)$ is a random number between 0 and 1. Here the following parameters are used: $h = 0.0085$, $dt = h$, $\epsilon = 0.0085$, $Pe = 1/\epsilon$, $Fr = 0.5$. The surface tension is omitted. It is worth pointing out that the density difference of the binary flows used here is small so that a Boussinesq approximation is applicable for the approximation [48,49]. As can be seen from Fig. 10, under the influence of buoyancy, the positions of binary fluid flows have changed along the helical collar surface. As we expected, the phase of small density, shown as blue part, moves upward while the one of big density moves reversely. This simulation indicates that our method can be effectively used for the computation with buoyancy-driven flow.

6. Conclusion

In this paper, we have proposed a second-order temporal and spatial accuracy, unconditionally energy stable numerical scheme, which is derived by coupling NS equation with the CH equation, to simulate the hydro-dynamic phase separation on arbitrarily curved surfaces. A novel surface discrete finite volume method was constructed for the high accuracy surface computation. Firstly, we constructed the discrete operators, i.e. discrete divergence, gradient, and Laplace–Beltrami operators, via a surface mesh consisting of triangular grids. Then the Crank–Nicolson method was applied in our scheme, which is embedded under the projection framework. We employed a Picard iteration to obtain a unique solution of pressure in NS equation. The resulting system of discrete equations was solved by the Jacobi-type iteration method and biconjugate gradient stabilized method. The proposed CHNS scheme was proved to be unconditionally energy stable. The mass conservation property was satisfied. To our knowledge, this was the first attempt to apply a second-order provably unconditionally stable scheme for the hydrodynamics coupled phase field model on the arbitrarily curved surfaces. We presented various results, such as the simulations with nonuniform and poor-quality meshes, shape relaxation on surfaces, phase deformation under shear flow, Kelvin–Helmholtz instability and simulation of buoyancy-driven flow, to demonstrate the robustness and efficiency of the proposed method.

Declaration of competing interest

The authors declare that they have no known competing financial interests or personal relationships that could have appeared to influence the work reported in this paper.

Acknowledgments

References

[1] D. Jeong, J. Kim, Conservative Allen–Cahn–Navier–Stokes system for incompressible two-phase fluid flows, Computers Fluids. 156 (2017) 239–246.

[2] M. Hintermüller, D. Wegner, Optimal control of a semidiscrete cahn–hilliard–Navier–Stokes system, SIAM J. Control Optim. 52 (2014) 747–772.

[3] F. Boyer, C. Laputerta, S. Minjeaud, B. Piar, M. Quintard, Cahn-hilliard/Navier–Stokes model for the simulation of three-phase flows, Transp. Porous Media. 82 (2010) 463–483.

[4] S. Minjeaud, An unconditionally stable uncoupled scheme for a triphasic Cahn-Hilliard/Navier–Stokes model, Numer. Methods Partial Differential Equations 29 (2013) 584–618.

[5] D. Kay, R. Welford, Efficient numerical solution of Cahn-Hilliard-Navier–Stokes fluids in 2d, SIAM J. Sci. Comput. 29 (2007) 2241–2257.

[6] Y. Li, H.G. Lee, B. Xia, J. Kim, A compact fourth-order finite difference scheme for the three-dimensional Cahn–Hilliard equation, Comput. Phys. Comm. 200 (2016) 108–116.

[7] Y. Li, J.I. Choi, J. Kim, Multi-component Cahn–Hilliard system with different boundary conditions in complex domains, J. Comput. Phys. 323 (2016) 1–16.

[8] B. Xia, C. Mei, Q. Yu, Y. Li, A second order unconditionally stable scheme for the modified phase field crystal model with elastic interaction and stochastic noise effect, Comput. Methods Appl. Mech. Engrg. 363 (2020) 112795.

[9] D. Jeong, J. Yang, J. Kim, A practical and efficient numerical method for the Cahn–Hilliard equation in complex domains, Commun. Nonlinear Sci. Numer. Simul. 73 (2019) 217–228.

[10] Z. Zhang, H. Tang, An adaptive phase field method for the mixture of two incompressible fluids, Computers Fluids 36 (2007) 1307–1318.

[11] F. Chen, J. Shen, Efficient energy stable schemes with spectral discretization in space for anisotropic Cahn–Hilliard systems, Commun. Comput. Phys. 13 (2013) 1189–1208.

[12] J. Kim, K. Kang, J. Lowengrub, Conservative multigrid methods for Cahn–Hilliard fluids, J. Comput. Phys. 193 (2004) 511–543.

[13] J. Shen, On error estimates of projection methods for Navier–Stokes equation: first order schemes, SIAM J. Numer. Anal. 29 (1992) 57–77.

[14] D. Han, X. Wang, A second order in time, uniquely solvable unconditionally stable numerical scheme for Cahn–Hilliard–Navier–Stokes equation, J. Comput. Phys. 290 (2015) 139–156.

[15] J. Shen, X. Yang, A phase-field model and its numerical approximation for two-phase incompressible flows with different densities and viscosities, SIAM J. Sci. Comput. 31 (2010) 1159–1179.

[16] J. Shen, X. Yang, Q. Wang, Mass and volume conservation in phase field models for binary fluids, Commun. Comput. Phys. 13 (2013) 1045–1065.

[17] Z. Guo, P. Lin, J.S. Lowengrub, A numerical method for the quasi-incompressible Cahn–Hilliard–Navier–Stokes equations for variable density flows with a discrete energy law, J. Comput. Phys. 276 (2014) 486–507.

[18] Y. Zhang, H. Wang, T. Tang, Simulating two-phase viscoelastic flows using moving finite element methods, Commun. Comput. Phys. 7 (2010) 333–349.

[19] H.Y. Lee, J. Lowengrub, J. Goodman, Modeling pinchoff and reconnection in a Hele-Shaw cell II. Analysis and simulation in the nonlinear regime, Phys. Fluids 14 (2) (2002) 514.

[20] C. Liu, J. Shen, A phase field model for the mixture of two incompressible fluids and its approximation by a fourier-spectral method, Physica D 179 (2003) 211–228.

[21] B.E. Griffith, An accurate and efficient method for the incompressible Navier–Stokes equations using the projection method as a preconditioner, J. Comput. Phys. 228 (2009) 7565–7595.

[22] L. Plasman, J. Deteix, D. Yakoubi, A projection scheme for Navier–Stokes with variableviscosity and natural boundary condition, Internat. J. Numer. Methods Fluids (2020) 1–21.

[23] M. Sun, X. Feng, K. Wang, Numerical simulation of binary fluid–surfactant phase field model coupled with geometric curvature on the curved surface, Comput. Methods Appl. Mech. Engrg. 367 (2020) 113–123.

[24] Y. Li, J. Choi, J. Kim, A phase-field fluid modeling and computation with interfacial profile correction term, Commun. Nonlinear Sci. Numer. Simul. 30 (2016) 84–100.

[25] S.G. Chen, J.Y. Wu, Discrete conservation laws on curved surfaces II: a dual approach, SIAM J. Sci. Comput. 36 (2014) 1813–1830.

[26] S.G. Chen, J.Y. Wu, Discrete conservation laws on curved surfaces, SIAM J. Sci. Comput. 36 (2013) 719–739.

[27] S.G. Chen, J.Y. Wu, Discrete conservation laws on evolving surfaces, SIAM J. Sci. Comput. 38 (2016) 1725–1742.

[28] S.J. Ruuth, B. Merriman, A simple embedding method for solving partial differential equations on surfaces, J. Comput. Phys. 227 (2008) 1943–1961.

[29] B. Merriman, S.J. Ruuth, Diffusion generated motion of curves on surfaces, J. Comput. Phys. 225 (2007) 2267–2282.

[30] C.B. Macdonald, J. Brandman, S.J. Ruuth, Solving eigenvalue problems on curved surfaces using the closest point method, J. Comput. Phys. 230 (2011) 7944–7956.

[31] Y. Li, J. Kim, N. Wang, An unconditionally energy-stable second-order time-accurate scheme for the Cahn–Hilliard equation on surfaces, Commun. Nonlinear Sci. Numer. Simul. 53 (2017) 213–227.

[32] M. Desbrun, A.N. Hirani, M. Leok, J.E. Marsden, Discrete exterior calculus, Mathematics 39 (2010) 2006.

[33] M.S. Mohamed, A.N. Hirani, R. Samtaney, Discrete exterior calculus discretization of incompressible Navier–Stokes equations over surface simplicial meshes, J. Comput. Phys. 312 (2016) 175–191.

[34] S. Reuther, A. Voigt, Solving the incompressible surface Navier–Stokes equation by surface finite elements, Phys. Fluids. 30 (2018) 012107.

[35] J. Yang, J. Kim, A phase-field model and its efficient numerical method for two-phase flows on arbitrarily curved surfaces in 3D space, Comput. Methods Appl. Mech. Engrg. 372 (2020) 113382.

[36] J. Yang, Y. Li, J. Kim, A practical finite difference scheme for the Navier–Stokes equation on curved surfaces in R^3, J. Comput. Phys. 411 (2020) 109403.

[37] E. Bänsch, J. Paul, A. Schmidt, An ALE finite element method for a coupled stefan problme and Navier–Stokes equations with free capillary surface, Internat. J. Numer. Methods Fluids 71 (2013) 1282–1296.

[38] E.H.V. Brummelen, B. Koren, Efficient numerical solution of steady free-surface Navier–Stokes flow, Modelling, Analysis and Simulation (MAS), J. Comput. Phys. 174 (2001) 120–137.

[39] T. Padmanabhan, Entropy density of spacetime and the Navier–Stokes fluid dynamics of null surfaces, Phys. Rev. D 83 (2010) 1–11.

[40] Y. Li, X. Qi, J. Kim, Direct discretization method for the Cahn–Hilliard equation on an evolving surface, J. Sci. Comput. 77 (2) (2018) 1147–1163.

[41] Y. Li, C. Luo, B. Xia, J. Kim, An efficient linear second order unconditionally stable direct discretization method for the phase-field crystal equation on surfaces, Appl. Math. Model. 67 (2019) 477–490.

[42] D. Han, A. Brylev, X. yang, Z. Tan, Numerical analysis of second order, fully discrete energy stable schemes for phase field models of two-phase incompressible flows, J. Sci. Comput. 70 (2017) 965–989.

[43] Y. Gong, J. Zhao, Q. Wang, An energy stable algorithm for a quasi-incompressible hydrodynamic phase-field model of viscous fluid mixtures with variable densities and viscosities, Commun. Comput. Phys. 219 (2017) 20–34.

[44] X. Pan, C. Lee, K. Kim, J. Choi, Analysis of velocity-components decoupled projection method for the incompressible Navier–Stokes equations, Comput. Math. Appl. 71 (2016) 1722–1743.

[45] D. Jeong, J. Kim, Microphase separation patterns in diblock copolymers on curved surfaces using a nonlocal Cahn–Hilliard equation, Eur. Phys. J. E. 38 (2015).

[46] J. Li, Q. Wang, A class of conservative phase field models for multiphase fluid flows, J. Appl. Mech. 81 (2014) 021004.

[47] H.G. Lee, J. Kim, Two-dimensional kelvin–helmholtz instabilities of multi-component fluids, Eur. J. Mech. B/Fluid 49 (2015) 77–88.

[48] Y. Gong, J. Zhao, X. Yang, Qi Wang, Fully discrete second-order linear schemes for hydrodynamic phase field models of binary viscous fluid flows with variable densities, SIAM J. Sci. Comput. 40 (2018) 138–167.

[49] H.G. Lee, J. Kim, A comparison study of the boussinesq and the variable density models on buoyancy-driven flows, J. Eng. Math. 75 (2012) 15–27.